

A superconducting qutrit link beyond the qubit limit

Xiang Li,^{1,2,3,*} Zheng-Yang Mei,^{1,2,†} Yang He,^{1,2} Si-Lu Zhao,^{1,2} Yan-Jun Liu,^{1,2} Xiao-Hui Song,^{1,4} Kai Xu,^{1,4,5} Zhong-Cheng Xiang,^{1,4} Dong-Ning Zheng,^{1,2,4,‡} and Heng Fan^{1,2,4,5,§}

¹*Beijing National Laboratory for Condensed Matter Physics,*

Institute of Physics, Chinese Academy of Sciences, Beijing 100190, China

²*School of Physical Sciences, University of Chinese Academy of Sciences, Beijing 100049, China*

³*Centre for Quantum Technologies, National University of Singapore, 117543, Singapore*

⁴*Hefei National Laboratory, Hefei 230088, China*

⁵*Beijing Academy of Quantum Information Sciences, Beijing 100193, China*

(Dated: June 30, 2026)

Superconducting microwave links have enabled deterministic state transfer and remote entanglement between qubits, but deterministic links have so far operated with an effectively two-dimensional transmitted Hilbert space. Here we demonstrate a superconducting qutrit link between two independently packaged nodes connected by a microwave channel. Each node combines a transmon qutrit, a transmission resonator, and a tunable Purcell-filter interface, allowing the two remote microwave-photon interfaces to be matched in both frequency and bandwidth. We implement two transition-selective photon-mediated operations that transfer the $|e\rangle$ and $|f\rangle$ qutrit components in distinct temporal modes of the same channel. We tomographically characterize arbitrary qutrit-state transfer, obtaining a mean transferred-state fidelity of 83.68% and a qutrit process fidelity of 77.12%, exceeding both the classical qutrit-transfer benchmark and the best possible average fidelity of an effective qubit channel used to transmit an arbitrary qutrit. Using partial-transfer operations, we reconstruct a remote two-qutrit state with negativity 0.730, a tomography-inferred dense-coding capacity of 2.273 bits, and a tomography-inferred Collins–Gisin–Linden–Massar–Popescu (CGLMP) parameter $I_3 = 2.332$, all beyond the corresponding qubit or local bounds. These results demonstrate a superconducting microwave link that uses the native three-level structure of transmons as a genuine high-dimensional communication resource.

I. INTRODUCTION

Coherent links between separated quantum systems are a basic ingredient of modular quantum processors and quantum networks [1, 2]. In such an architecture, small processors can be fabricated, controlled and diagnosed as separate units, while itinerant carriers distribute quantum states and entanglement between them. Most experimental links encode one qubit per carrier or per node, but a larger local Hilbert space can change what a network link can transmit. A qutrit carries a three-dimensional quantum state, and two qutrits can host entanglement with Schmidt rank three, which cannot be embedded in any two-qubit state. Such high-dimensional resources can increase dense-coding capacity, support qudit Bell inequalities and provide a larger alphabet for quantum communication, quantum computation and quantum metrology [3–7]. In optics, high-dimensional photonic states have become a central resource for quantum communication protocols [8–11]. High-dimensional qudits have also been controlled and entangled in local trapped-ion processors and solid-state spin registers [12–14], demonstrating the hardware potential of qutrit and

qudit encoding. Extending this capability from local processors to remote nodes, however, requires a link that can transfer and entangle full three-level quantum states rather than a single two-level subspace. At the network level, such resources could also enable high-dimensional Bell-type protocols with ternary outcomes, extending recent superconducting-circuit demonstrations of loophole-free Bell tests and device-independent randomness amplification from binary qubit correlations toward qutrit correlations [15, 16].

Superconducting circuits provide a natural platform for testing whether this high-dimensional network picture can be made deterministic in the microwave domain. Circuit QED combines strong artificial atom-resonator coupling with shaped microwave emission and time-reversed capture [17], enabling deterministic state transfer and remote entanglement between superconducting qubits and microwave cavity memories [18–24]. At the same time, the higher transmon levels are native degrees of freedom rather than added hardware, and local qutrit control, benchmarking and multi-qutrit gates have developed rapidly [25–30]. A remote qutrit link, however, requires more than reusing a qubit link with a larger local basis. It must map the two non-ground amplitudes onto two temporal modes of the same waveguide, preserve their calibrated relative phase, and avoid opening all qutrit transitions to the continuum at once.

Here we demonstrate qutrit-level quantum communication between two independently packaged superconducting nodes connected by a one-metre microwave link.

* These authors contributed equally to this work.; francis_li@nus.edu.sg

† These authors contributed equally to this work.

‡ dzheng@iphy.ac.cn

§ hfan@iphy.ac.cn

Each node contains a transmon qutrit, an auxiliary resonator and a tunable Purcell-filter interface. The auxiliary resonator provides a transition-selective interface between the stored qutrit and the travelling microwave field: only the addressed qutrit–resonator sideband is opened, while the other qutrit amplitude remains stored in the transmon. This is the key difference from a direct qubit–waveguide interface, where opening the radiative channel generally exposes all allowed transmon transitions to the same continuum. The Purcell filter controls the coupling decay rate κ_c from the auxiliary resonator into the waveguide, while the transmon flux bias controls the dressed auxiliary-resonator frequency through the dispersive Lamb shift. With these two knobs we match both the resonant frequency and the photon bandwidth of the two remote interfaces in situ [31]. We then send the qutrit amplitude in two time bins through the same cascaded channel, using an $e0g1$ flux-parametric sideband [32] for the $|e\rangle$ component and an $f0g1$ cavity-assisted Raman process [20, 22, 33] for the $|f\rangle$ component.

The results cross the qubit boundary in three experimentally reconstructed ways. First, qutrit state transfer gives a mean transferred-state fidelity of 83.68%, above the classical qutrit measure-and-prepare limit $1/2$ and the maximum average fidelity $3/4$ for transmitting an arbitrary qutrit through an effective two-dimensional channel. Quantum process tomography of the same transfer protocol gives $F_\chi = 77.12\%$, above the corresponding process-fidelity bounds $1/3$ and $2/3$ [34, 35]. Second, by reducing the primitive pulse areas, the same hardware generates a remote two-qutrit maximally entangled state $(|gf\rangle + |ee\rangle + |fg\rangle)/\sqrt{3}$: its fidelity exceeds the Schmidt-rank-two bound $2/3$, and its negativity is 0.730, above the maximum 0.5 for any two-qubit state [36–39]. Third, the reconstructed ensemble-averaged density matrix gives a tomography-inferred dense-coding capacity of 2.273 bits, above the classical qutrit value $\log_2 3$ and the ideal qubit dense-coding limit of 2 bits [3–5], together with a tomography-inferred Collins–Gisin–Linden–Massar–Popescu (CGLMP) Bell parameter $I_3 = 2.332$, above the local bound of 2 [6]. These measurements show that the same microwave link can act as a coherent three-level channel and as a source of high-dimensional entanglement.

II. TUNABLE-INTERFACE ARCHITECTURE AND QUTRIT PROTOCOL

The device architecture is shown schematically in Fig. 1a. The two superconducting nodes are mounted in separate sample boxes and connected by a one-metre microwave cable. Each node contains a transmon qutrit [40], with logical states $\{|g\rangle, |e\rangle, |f\rangle\}$, and a transmission resonator that emits and captures itinerant photons. A tunable Purcell filter couples the transmission resonator to the cascaded waveguide [41–43]. The resulting interface has two independent matching knobs.

The transmon flux bias shifts the dressed transmission-resonator frequency through the dispersive Lamb shift, while the Purcell-filter bias changes the loaded linewidth and hence the photon bandwidth. We use these knobs to bring the two remote interfaces to a common operating frequency near 7.4347 GHz and to choose comparable radiative linewidths; the corresponding spectroscopy and linewidth data are given in Supplementary Figs. S4 and S5.

The qutrit channel is built from two transition-selective photon-mediated primitives, labelled $e0g1$ and $f0g1$, as illustrated in Fig. 1b,c. The $e0g1$ primitive couples $|e, 0\rangle$ and $|g, 1\rangle$ of a single node, where the second label denotes the photon number in the transmission resonator. We implement this coupling by applying a flux-parametric modulation to the transmon at the qubit–transmission-resonator detuning frequency [32, 44]. In the rotating frame, this modulation activates an effective sideband interaction that converts a transmon $|e\rangle$ excitation into one transmission-resonator photon, or the reverse process. In the link experiment, this sideband turns the transmission resonator into a temporary output interface for the $|e\rangle$ amplitude: node A emits the photon, and a time-delayed partner pulse at node B absorbs the same temporal mode into the remote transmon.

The $f0g1$ primitive addresses the $|f\rangle$ component through a cavity-assisted Raman process, like the Raman-type microwave reset and photon-mediated transfer protocols in circuit QED [20, 22, 33]. The Raman control couples $|f, 0\rangle$ to $|g, 1\rangle$ through the transmission-resonator mode while the $|e\rangle$ amplitude is left largely stored. The transmission resonator therefore plays a dual role: it is the impedance-matched port to the waveguide, and it is the intermediate mode that makes the port transition selective. This allows the $|e\rangle$ and $|f\rangle$ amplitudes to be emitted and captured in different time windows without adding a second physical channel.

Both primitives are implemented with chirped 200 ns sine pulses. The sine envelope shapes the emitted microwave field into a near time-symmetric temporal mode, so that a delayed partner pulse with the same envelope approximates time-reversed capture at the receiver. The chirp compensates the amplitude-dependent transition-frequency shift during the pulse: for $e0g1$, this shift comes mainly from the flux-modulation-induced time-averaged transmon-frequency shift, while for $f0g1$ it comes mainly from the Raman-drive-induced ac Stark shift. The chirp profiles are independently calibrated from amplitude-to-frequency measurements for the two primitives, as shown in Supplementary Fig. S6. Full-transfer $e0g1$ and $f0g1$ operations implement the qutrit state-transfer map in Fig. 1d, while partial-transfer operations generate the time-bin-mediated entanglement resource shown in Fig. 1e. The calibrated receiver-pulse delays are 8 ns for $e0g1$ and 13 ns for $f0g1$.

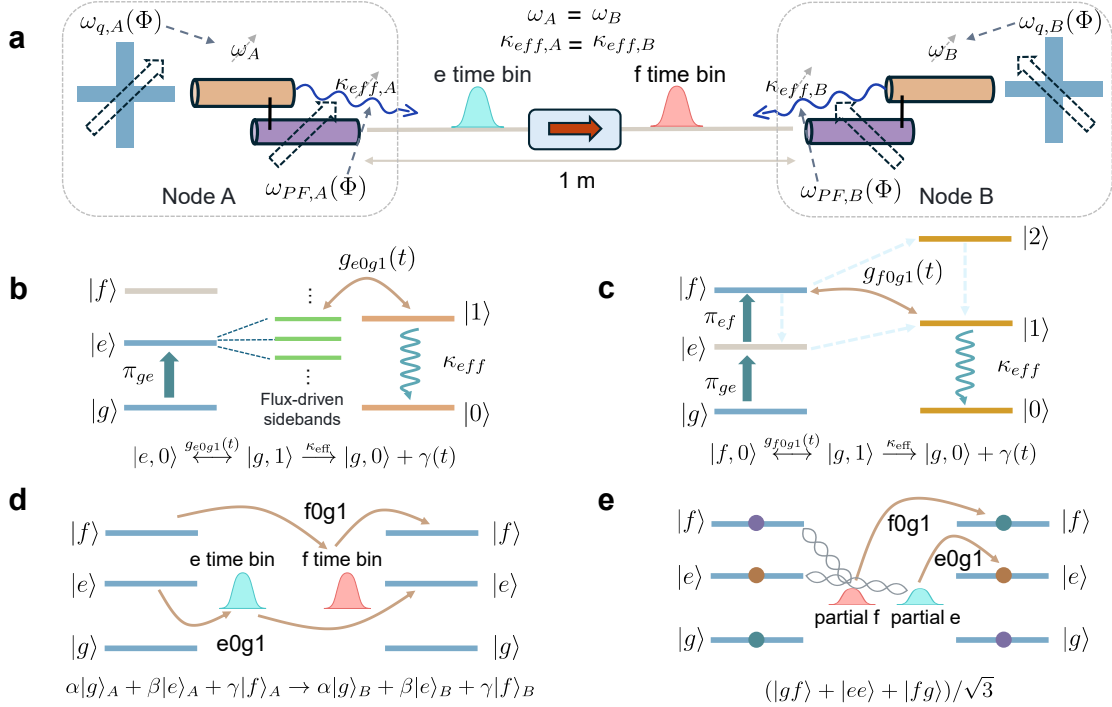


FIG. 1: **Remote qutrit communication between independently packaged superconducting nodes.** (a) Two independently packaged superconducting nodes are connected by a one-metre cascaded microwave link. Each node contains a transmission qutrit, a transmission resonator and a tunable Purcell-filter interface. The transmon flux bias tunes the dressed transmission-resonator frequency, while the Purcell-filter bias tunes the radiative linewidth, allowing the two remote interfaces to be matched in both frequency, $\omega_A = \omega_B$, and photon bandwidth, $\kappa_{\text{eff},A} = \kappa_{\text{eff},B}$. The two non-ground qutrit amplitudes are carried by two temporal modes of the same link. (b) The $e0g1$ primitive is a flux-driven sideband that couples $|e, 0\rangle$ and $|g, 1\rangle$, followed by emission through κ_{eff} . (c) The $f0g1$ primitive uses a cavity-assisted Raman process to couple $|f, 0\rangle$ and $|g, 1\rangle$. (d) Combining the two primitives in b and c as full-transfer operations transfers an arbitrary qutrit state from node A to node B using two time bins. (e) Using the same two primitives as partial-transfer operations first entangles node A with the itinerant time-bin modes; absorption by node B maps this resource into the remote two-qutrit state $(|gf\rangle + |ee\rangle + |fg\rangle)/\sqrt{3}$.

III. PRIMITIVES OF MICROWAVE QUTRIT TRANSFER

We first calibrate the elementary remote links by measuring their population dynamics. In Fig. 2, the $|e0\rangle \leftrightarrow |g1\rangle$ and $|f0\rangle \leftrightarrow |g1\rangle$ transfers are plotted as a function of pulse time. Node A emits the excitation with a chirped 200 ns sine pulse; node B applies the time-delayed partner pulse to absorb the same temporal mode. The sine envelope smooths the turn-on and turn-off of the effective coupling and produces a near-symmetric photon wavepacket for the calibrated bandwidth. The receiver pulse starts 8 ns after the sender pulse for $e0g1$ and 13 ns after the sender pulse for $f0g1$; the population traces are shown on the same measured cutoff-time axis. This is the microwave analogue of shaped-photon emission and time-reversed capture [45–47]. The solid curves come from a pulse-level cascaded master-equation simulation implemented with QuTiP [48–51]. The model

uses the measured energy-relaxation rates, $\eta_c = 0.92$, $\kappa_{\text{int},A}/2\pi = 0.0208$ MHz, $\kappa_{\text{int},B}/2\pi = 0.0176$ MHz, and a T_1 -corrected quasi-static $1/f$ -like dephasing ensemble extracted from Ramsey data. The effective peak couplings used for the simulations in Figs. 2–4 are listed in the Supplementary Information; within each QPT or QST simulation these calibrated pulse parameters are held fixed across all prepared and measured states.

We characterize the two primitives as separate effective two-level transfer channels. The $e0g1$ primitive transfers the $\{|g\rangle, |e\rangle\}$ component through the $|e, 0\rangle \leftrightarrow |g, 1\rangle$ sideband, whereas the $f0g1$ primitive transfers the $\{|g\rangle, |f\rangle\}$ component through the Raman-assisted $|f, 0\rangle \leftrightarrow |g, 1\rangle$ channel. Two-level process tomography gives $F_\chi = 89.66 \pm 0.29\%$ for $e0g1$ and $85.68 \pm 0.60\%$ for $f0g1$. The corresponding mean output-state fidelities, in the same order, are $93.23 \pm 0.19\%$ and $90.45 \pm 0.27\%$. These independently calibrated operations are the two building blocks combined below for full qutrit transfer.

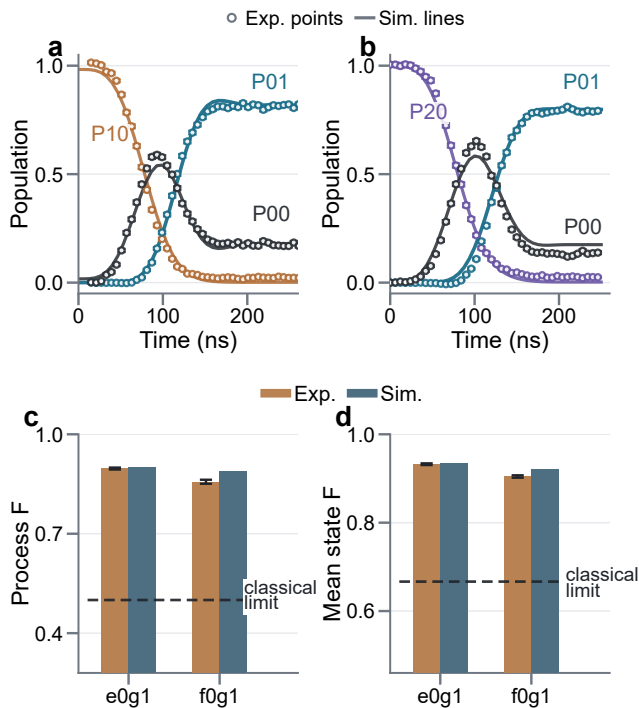


FIG. 2: **Primitive transfer dynamics and two-level process benchmarks.** (a,b) Readout-corrected population dynamics for the $e0g1$ and $f0g1$ transfer primitives, with experimental data shown with error bars and solid curves from the pulse-level cascaded master-equation simulation. (c,d) Process-tomography benchmarks for the two primitive transfer channels. The shaded regions and dashed reference lines mark the classical two-level process-fidelity benchmark $F_{\text{proc}} = 1/2$ in c and the corresponding mean-state-fidelity benchmark $F_{\text{avg}} = 2/3$ in d.

IV. ARBITRARY QUTRIT-STATE TRANSFER

The full qutrit-transfer sequence applies the two primitives in separate temporal windows. Node A is prepared in the qutrit state to be sent and node B starts in $|g\rangle$. The $f0g1$ sender pulse first maps the $|f\rangle_A$ amplitude onto a single photon in the first temporal mode; the $e0g1$ sender pulse then maps the $|e\rangle_A$ amplitude onto a single photon in the second temporal mode. The $|g\rangle_A$ component is dark to both primitives and is represented by the joint vacuum of the two time bins. The flying field therefore carries a hybrid number–time-bin qutrit,

$$\alpha |0_1 0_2\rangle + \gamma e^{i\varphi_f} |1_1 0_2\rangle + \beta e^{i\varphi_e} |0_1 1_2\rangle, \quad (1)$$

where 1 and 2 label the $f0g1$ and $e0g1$ time windows, respectively. Node B applies the time-reversed capture pulses to convert the first-bin photon to $|f\rangle_B$ and the second-bin photon to $|e\rangle_B$. In the ideal limit,

$$|e\rangle_A |g\rangle_B \rightarrow |g\rangle_A |e\rangle_B, \quad |f\rangle_A |g\rangle_B \rightarrow |g\rangle_A |f\rangle_B, \quad (2)$$

while $|g\rangle_A |g\rangle_B$ remains dark to both transfer pulses. After the two windows, $\alpha |g\rangle_A + \beta |e\rangle_A + \gamma |f\rangle_A$ is mapped to node B, up to deterministic phases removed with calibrated drive phases and virtual- Z gates. The pulse ordering, delay scans and phase calibrations are provided in Supplementary Fig. S7.

Qutrit state tomography uses nine analysis rotations before three-state readout, and qutrit process tomography combines nine independently prepared input states with the corresponding readout-corrected output density matrices. The channel is reconstructed in the Gell-Mann basis [52–54]. Figure 3 compares the experimental process matrix with the pulse-level simulation and the ideal identity process in a compact overlaid representation; the complementary imaginary components and matrix-distance diagnostics are given in the Supplementary Information. The dominant identity component shows that the two time-bin primitives preserve a common qutrit phase frame, rather than acting as two independent population transfers. The residual off-diagonal terms give the remaining phase errors, leakage and dephasing accumulated during emission, propagation and capture.

Across the tested input states, the mean transferred-state fidelity is $83.68 \pm 0.04\%$, above the classical qutrit measure-and-prepare limit of 50% and above the maximum average fidelity 75% achievable by transmitting an arbitrary qutrit through an effective qubit channel [34, 35]. The measured qutrit process fidelity is $77.12 \pm 0.10\%$. The same pulse-level cascaded simulation gives a process fidelity of 84.10% and a mean state fidelity of 89.45%, higher than the experimental values. As a separate process-matrix comparison, the matrix-distance measure $D(\chi, \chi_{\text{sim}}) = \sqrt{\text{Tr}[(\chi - \chi_{\text{sim}})^2]}$, used in microwave-link process comparisons [20], gives $D = 0.141$ between the measured and simulated qutrit process matrices. The remaining experiment–simulation differences are consistent with residual calibration errors and slow parameter drifts during the long qutrit QPT acquisition that are not included in the fixed-parameter model.

V. REMOTE QUTRIT ENTANGLEMENT BEYOND THE QUBIT LIMIT

Remote entanglement generation uses the same photon-mediated operations before they reach complete population exchange, but the sequence is a three-path interference protocol rather than two independent partial transfers. Unlike the full-transfer sequence in Fig. 3, the REG sequence starts with the $e0g1$ branch and then applies the $f0g1$ branch, because the first operation must split the initial $|e\rangle_A$ amplitude while leaving a stored component for subsequent relabelling. A partial $e0g1$ operation first creates one branch that will be absorbed as $|e\rangle_B$, while the remaining amplitude stays stored in node A. Local π_{ef} and π_{ge} rotations relabel the stored branches, and a subsequent partial $f0g1$ operation splits the remaining stored amplitude into a no-photon branch

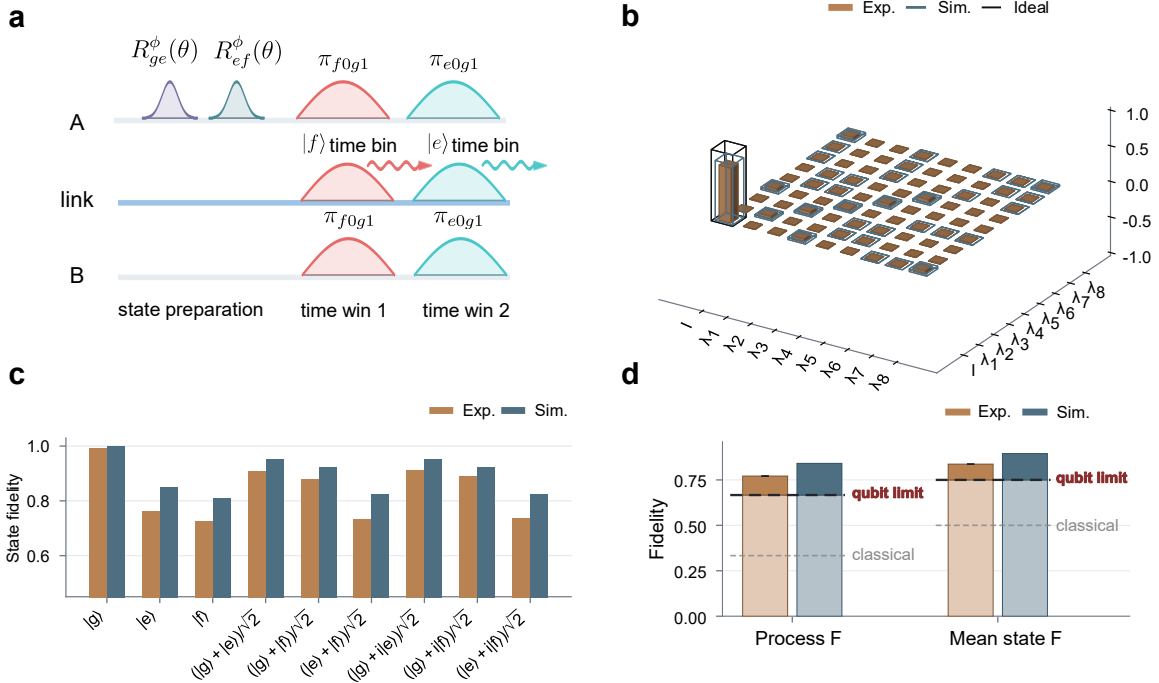


FIG. 3: **Arbitrary qutrit-state transfer through the microwave link.** (a) Pulse-sequence schematic for transferring the two non-ground qutrit components with the $f0g1$ and $e0g1$ photon-mediated primitives. Here $R_{ge}^\phi(\theta)$ and $R_{ef}^\phi(\theta)$ denote rotations by angle θ about an axis set by phase ϕ in the equatorial plane of the ge and ef subspaces, respectively. In the state-transfer sequence, the π_{f0g1} pulse maps the $|f\rangle$ amplitude to the first time-bin photon, and the π_{e0g1} pulse maps the $|e\rangle$ amplitude to the second time-bin photon. (b) Real part of the experimental, simulated and ideal qutrit process matrix in the Gell-Mann basis. This overlaid matrix view is intended to show the dominant identity-process structure; complementary imaginary components and quantitative matrix-distance diagnostics are provided in the Supplementary Information. (c) Transferred-state fidelities for representative qutrit input states. (d) Mean state fidelity and process fidelity compared with the classical qutrit benchmark and the qubit-channel limit.

and a second-bin photon branch. After full capture, the three coherent alternatives become $|fg\rangle$, $|ee\rangle$ and $|gf\rangle$, giving $(|gf\rangle + |ee\rangle + |fg\rangle)/\sqrt{3}$ up to local phases. Because the flying state contains the vacuum, a first-bin photon or a second-bin photon, but no $|1_1 1_2\rangle$ two-photon component, at most one photon is exposed to propagation loss in the link. The two-qutrit state is reconstructed from the tensor product of the single-qutrit tomography settings, giving 81 joint analysis settings. The density matrix in Fig. 4 contains the corresponding experimental and simulated reconstructions, with $D(\rho, \rho_{\text{sim}}) = 0.119$. The three target populations and the three pairwise coherences dominate the reconstruction, which is the signature of a coherent two-qutrit Bell state rather than an incoherent mixture of transferred populations.

The state fidelity is $81.21 \pm 0.37\%$. This exceeds the maximum overlap $2/3$ between the target maximally entangled qutrit state and any Schmidt-rank-two state, and therefore witnesses Schmidt number 3 [36]. The ensemble-averaged density matrix gives a negativity of 0.730 ± 0.005 , above the two-qubit maximum 0.5 [37–

39]. All quoted REG metrics use independently calibrated readout-assignment corrections; their robustness to assignment-matrix uncertainty is quantified in the Supplementary Information. We then evaluate the communication metrics of the same averaged reconstructed state [3–6]. The tomography-inferred dense-coding capacity is 2.273 ± 0.014 bits, larger than both the classical qutrit value $\log_2 3 = 1.585$ bits and the ideal qubit dense-coding limit of 2 bits. The tomography-inferred CGLMP parameter is $I_3 = 2.332 \pm 0.012$, above the local realistic bound. Using the same averaged-density-matrix convention, the corresponding simulated values are $F = 0.834$, $\mathcal{N} = 0.756$, $C = 2.242$ bits and $I_3 = 2.417$. This fixed-parameter simulation is used as a consistency check of the reconstructed state structure rather than as a fitted upper bound on the REG benchmarks. These four quantities probe different aspects of the same reconstructed state: overlap with a rank-three target, entanglement dimensionality, communication capacity and nonlocal-correlation strength.

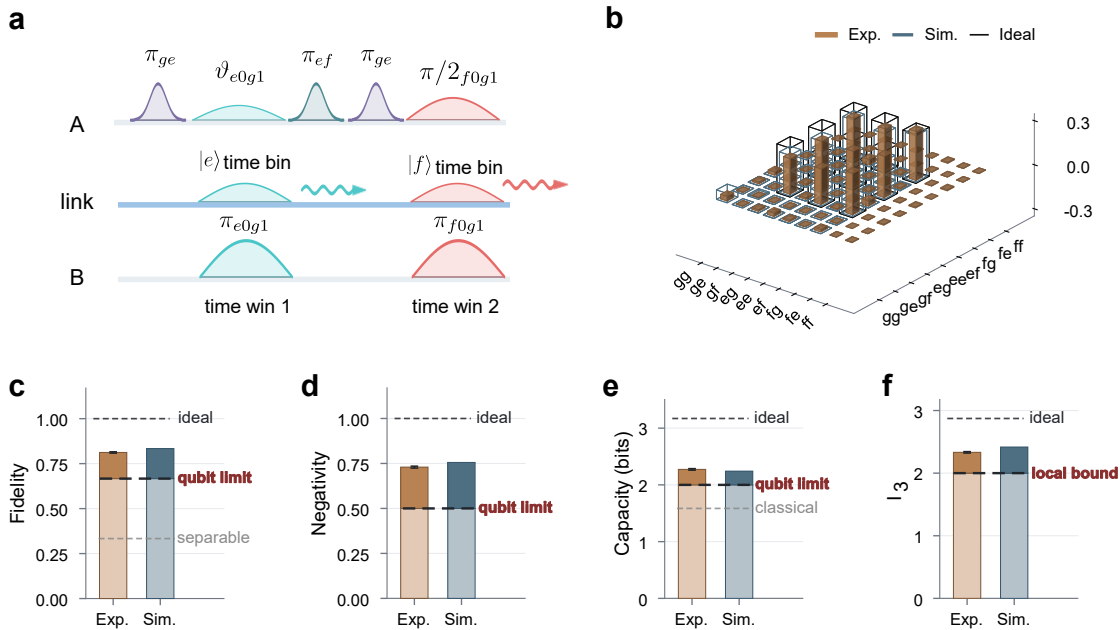


FIG. 4: **Remote qutrit entanglement beyond the qubit limit.** (a) Pulse-sequence schematic for generating remote qutrit entanglement with partial $e0g1$ and $f0g1$ transfers. In this REG sequence, $e0g1$ creates the first time-bin branch and $f0g1$ creates the second time-bin branch; this ordering is distinct from the full qutrit-transfer sequence in Fig. 3. The $e0g1$ pulse angle is set to $\vartheta_{e0g1} = 2 \arctan(1/\sqrt{2})$, corresponding to a target transfer probability of $1/3$ for the $|e\rangle$ population into the first time-bin photon. The $f0g1$ pulse angle is set to $\vartheta_{f0g1} = \pi/2$, corresponding to a target transfer probability of $1/2$ for the $|f\rangle$ population into the second time-bin photon. (b) Real part of the experimental, simulated and ideal density matrix of the generated two-qutrit state after local phase alignment. The overlaid view highlights the target populations and coherences; complementary imaginary-part, matrix-distance and readout-correction robustness diagnostics are provided in the Supplementary Information. (c-f) State fidelity, negativity, tomography-inferred dense-coding capacity and tomography-inferred CGLMP parameter compared with the relevant classical, qubit or local bounds.

VI. DISCUSSION AND CONCLUSION

The experiment demonstrates coherent qutrit-state transfer and remote qutrit entanglement between two separately packaged superconducting nodes. The central control problem is not simply to increase the local Hilbert-space dimension, but to expose that Hilbert space to a travelling channel one transition at a time. The tunable Purcell filters set the radiative linewidths of the auxiliary resonators, while the transmon flux biases set their dressed frequencies. This combination lets the $e0g1$ and $f0g1$ photons occupy the same directional channel, with matched bandwidths and a stable relative phase. A pulse-level cascaded master-equation model, using measured relaxation, internal resonator loss, finite channel efficiency and T_1 -corrected quasi-static $1/f$ -like detuning noise, reproduces the measured population dynamics and gives the scale of the tomography benchmarks.

The auxiliary resonator is the element that makes this qutrit mapping selective. The quantum state is

stored in the transmon levels, while the auxiliary resonator is turned into an itinerant-photon interface only for the addressed transition. The $e0g1$ pulse opens the $|e, 0\rangle \leftrightarrow |g, 1\rangle$ manifold and leaves the $|f\rangle$ amplitude stored; the $f0g1$ pulse opens the $|f, 0\rangle \leftrightarrow |g, 1\rangle$ manifold and leaves the $|e\rangle$ amplitude stored. The two non-ground qutrit amplitudes are therefore converted into two separated temporal modes of the same microwave channel. In a direct transmon-waveguide geometry, opening the radiative channel would expose all allowed transitions to the continuum at once, making this time-windowed qutrit encoding difficult without additional filtering. The present architecture separates memory, transition selection and waveguide coupling into different physical elements.

This selectivity is not tied to a single implementation of the sideband interaction. In the present device, the $e0g1$ primitive is activated by flux modulation of a tunable transmon, and the $f0g1$ primitive is implemented as a cavity-assisted Raman process. More generally, the

same logical operation only requires a controllable sideband between a chosen qutrit transition and the transmission resonator. Such sidebands can also be driven in fixed-frequency circuits, where an off-resonant microwave drive stimulates shaped photon emission at a tunable photon frequency without changing the circuit parameters [55]. Thus the protocol is not tied to flux-tunable transmons: fixed-frequency processors could implement the same time-bin qutrit link if the two qutrit transitions can be coupled selectively to shaped emission and capture, with a calibrated relative phase between the two time bins.

The evidence for operation beyond the qubit limit appears at three levels. First, the average transferred-state fidelity exceeds both the classical qutrit benchmark and the best possible average fidelity of a two-dimensional channel used to transmit an arbitrary qutrit. Second, the generated two-qutrit state has a negativity above the two-qubit maximum, and its target-state fidelity witnesses Schmidt number 3. Third, the same density matrix gives a tomography-inferred dense-coding capacity above the ideal qubit limit and a tomography-inferred CGLMP value above the local realistic bound. These benchmarks test different failure modes: loss of qutrit coherence during transfer, collapse of the entangled state into a two-dimensional subspace, and loss of the information advantage expected from a high-dimensional resource.

The dense-coding and CGLMP numbers should be read in this calibrated-tomography sense. They are not yet a direct dense-coding experiment or a loophole-free Bell test. They show, instead, that the generated density matrix has the structure needed for those protocols. From one maximally entangled qutrit pair, local qutrit gates on the sender side generate the nine orthogonal generalized Bell states $\{(X^m Z^n \otimes I) |\Phi_3\rangle\}_{m,n=0}^2$, with $|\Phi_3\rangle = (|00\rangle + |11\rangle + |22\rangle)/\sqrt{3}$. The inferred capacity therefore quantifies how close the present state is to a usable three-level dense-coding resource. Likewise, the CGLMP value identifies the measurement basis and state quality required for a future direct high-dimensional Bell experiment. Loophole-free Bell tests with remote superconducting qubits have already been realized [15]; the present experiment indicates how such an architecture could be extended from a two-outcome CHSH setting to a three-outcome qutrit measurement. At the current operating point the dominant limitations are finite channel efficiency, qutrit relaxation and low-frequency phase noise, while internal transmission-resonator loss gives a smaller but systematic contribution. Higher channel efficiency, longer qutrit coherence, reduced low-frequency phase noise and improved REG waveform design should therefore increase both the transfer fidelity and the dense-coding capacity.

This conclusion is supported by the simulation error budget and by forward simulations using improved waveform choices in the full cascaded transmission-resonator model, as detailed in the Supplementary Information.

Under projected device parameters $\eta_c = 0.98$, $T_1 = 50 \mu\text{s}$ for both addressed qutrit transitions, Markovian $T_\phi = 20 \mu\text{s}$, and no additional internal transmission-resonator loss, an unwindowed sech emission-and-capture pulse, $g(t) = g_0/\cosh[(t-t_0)/\tau]$ with $g_0/2\pi = 1/(2\pi\tau) = 5 \text{ MHz}$, gives a mean qutrit-transfer state fidelity of 0.968 and a qutrit process fidelity of 0.948 in the pulse-level model. For REG, the corresponding waveform is obtained from the finite-resonator input-output equations by choosing a smooth emitted mode and solving for the capture controls, with the receiver control allowed to enter the capture window at finite coupling. A representative 200 ns REG waveform constrained to $g_{\text{max}}/2\pi = 3.95 \text{ MHz}$ under the same projected device parameters gives a REG state fidelity of 0.939, negativity 0.909, tomography-inferred dense-coding capacity 2.718 bits and tomography-inferred $I_3 = 2.688$. These projected values remain above the Schmidt-rank-two, two-qubit, dense-coding and local bounds with substantial margins, indicating that improved channel efficiency, longer qutrit coherence and REG waveform optimization would move the platform from a proof-of-principle high-dimensional link toward a higher-fidelity qutrit-network primitive.

The protocol increases the transmitted Hilbert-space dimension without adding another physical link. The same principle can be extended to higher transmon levels, to cavity-encoded qudits, or to multi-node microwave networks in which high-dimensional entanglement is distributed as a resource for modular gates and communication. The key requirement is a matched, tunable interface that can release and absorb different logical amplitudes in controlled temporal modes, while keeping the unused amplitudes protected in a local memory.

VII. METHODS

A. Device and microwave-link configuration

Each node consists of a flux-tunable transmon qutrit, an auxiliary resonator for photon emission and capture, a readout resonator, and a tunable Purcell-filter interface to the waveguide. The two nodes are mounted in separate sample boxes and connected by a one-metre microwave cable. The asymmetric-junction transmons provide a broad frequency tuning range while retaining the lowest three levels as the qutrit manifold. The auxiliary-resonator frequency is adjusted through the transmon-induced dispersive Lamb shift, and the external coupling rate is adjusted through the Purcell-filter bias. The sample layout, cryogenic wiring and device parameters are given in Supplementary Figs. S1–S3 and Supplementary Table S1.

B. Frequency and linewidth matching

Efficient photon-mediated transfer requires both frequency matching and bandwidth matching between the two remote interfaces. We first use cavity spectroscopy to track the flux-dependent auxiliary-resonator frequencies of the two nodes. Because the spectroscopy background changes with flux, the maps are background corrected line by line before ridge extraction. The final transfer frequency is determined from matched line cuts and lies near 7.4347 GHz. The smooth curves in Supplementary Fig. S4 are used only as visual guides for the flux-dependent cavity trajectories and are not used to define the final operating frequency.

The Purcell-filter control is calibrated by preparing one photon in the auxiliary resonator and measuring the cavity-energy decay as a function of the filter z -pulse amplitude. Each trace is fitted to

$$P_1(t) = P_{\text{off}} + A \exp(-t/T_{\text{cav}}), \quad (3)$$

and the loaded coupling decay rate is reported as

$$\kappa/2\pi = \frac{1}{2\pi T_{\text{cav}}}. \quad (4)$$

The nearest directly measured high-bandwidth settings used in the experiment are $z_A = 0.37$, giving $\kappa_A/2\pi = 10.72 \pm 0.44$ MHz, and $z_B = 0.21$, giving $\kappa_B/2\pi = 10.28 \pm 0.26$ MHz. The full linewidth calibration, including the finite square-pulse response at the largest coupling settings, is shown in Supplementary Fig. S5.

C. Parametric transfer primitives

The elementary transfer primitives are implemented with flux-parametric modulation of the qutrit-resonator interaction. The $e0g1$ pulse couples $|e, 0\rangle$ and $|g, 1\rangle$, while the $f0g1$ pulse couples $|f, 0\rangle$ and $|g, 1\rangle$. The emitted photon from node A propagates through the directional microwave channel and is captured by the corresponding pulse on node B. The pulses have a 200 ns sine amplitude envelope in the experiment. This envelope is used as a practical photon-shaping pulse: it produces an approximately time-symmetric itinerant mode for matched emission and capture, while avoiding the abrupt spectral components of a square pulse. The sender pulse defines the start of the primitive. The receiver pulse starts 8 ns after the sender pulse for $e0g1$ and 13 ns after the sender pulse for $f0g1$, compensating the propagation delay and the calibrated temporal offset between emission and absorption. All measured populations in Fig. 2 are compared at the same physical cutoff time. For a full primitive, the pulse amplitudes are set near the first maximum of the transfer population. In the small-amplitude regime used for partial primitives, the $e0g1$ flux-drive amplitude and the $f0g1$ Raman-drive amplitude are proportional to

the corresponding effective resonant coupling strengths, so reducing the programmed amplitude reduces the pulse area and stops the exchange at the desired population splitting.

The microwave frequency is chirped during each primitive pulse. For $e0g1$, the flux-parametric modulation changes the average transmon frequency during the pulse, so a fixed modulation frequency would move away from the instantaneous sideband resonance. For $f0g1$, the cavity-assisted Raman drive produces an amplitude-dependent ac Stark shift. We calibrate these shifts by sweeping pulse amplitude and drive frequency for each node and primitive, extracting the resonance ridge, and converting the calibrated ridge into an instantaneous frequency program $\omega_d[A(t)]$ for the sine envelope. The pulse-level simulations are evaluated in this chirp-corrected resonant frame; residual detuning is included through the measured slow-dephasing model.

For the primitive population and two-level QPT data, the measured levels are chosen according to the addressed subspace. In the $f0g1$ primitive, an additional calibrated π_{ef} mapping pulse is applied before readout when the analysis is performed in the $\{|g\rangle, |e\rangle\}$ readout basis. This mapping does not change the physical transfer primitive; it only maps the receiver $|f\rangle$ population to a level that is read out with higher contrast in that calibration.

D. Qutrit state transfer and entanglement sequences

Arbitrary qutrit-state transfer is obtained by applying the two primitive transfer operations to the non-ground components of the input state. Each experimental run starts with both nodes reset to $|g\rangle$. A local preparation sequence on node A generates one of the qutrit input states used for QST or QPT, while node B remains in $|g\rangle$. The transfer sequence then applies the two time-delayed sender-receiver pulse pairs. In the sequence used for Fig. 3, the $f0g1$ pair is applied first and transfers the $|f\rangle_A$ amplitude through the first time bin; the $e0g1$ pair is applied second and transfers the $|e\rangle_A$ amplitude through the second time bin. The $|g\rangle_A$ component is not resonant with either primitive and remains the two-bin vacuum component of the transfer channel. The ideal transfer maps

$$\alpha |g\rangle_A + \beta |e\rangle_A + \gamma |f\rangle_A \rightarrow \alpha |g\rangle_B + \beta e^{i\phi_e} |e\rangle_B + \gamma e^{i\phi_f} |f\rangle_B, \quad (5)$$

where the phases ϕ_e and ϕ_f are removed by calibrated virtual- Z rotations. The input states used for qutrit process tomography are generated by local qutrit rotations in the $|g\rangle$ - $|e\rangle$ and $|e\rangle$ - $|f\rangle$ subspaces. The tomography procedure, readout correction and basis convention are described in the Supplementary Information.

Remote entanglement generation uses partial transfer operations derived from the same $e0g1$ and $f0g1$ primitives. The experiment again starts from node B ini-

tialized in $|g\rangle$, while node A is locally prepared for the entangling sequence. In the ideal lossless map, a local π_{ge} pulse prepares $|e\rangle_A$. An $e0g1$ partial-transfer pulse with angle $2 \arctan(1/\sqrt{2})$ creates a $1/\sqrt{3}$ first-bin photon branch and a $\sqrt{2/3}$ stored branch. Local π_{ef} and π_{ge} rotations then relabel the stored branches, and a subsequent $f0g1$ partial-transfer pulse with angle $\pi/2$ divides the remaining stored amplitude into a no-photon branch and a second-bin photon branch. The receiver uses full $e0g1$ and $f0g1$ capture pulses to map the first and second time bins to $|e\rangle_B$ and $|f\rangle_B$, respectively. The calibrated experimental pulse amplitudes and virtual- Z phases implement the same three-path interference condition after accounting for loss, finite capture efficiency and phase accumulation. The sequence is calibrated to generate the target state

$$|\Psi_{\text{qutrit}}\rangle = \frac{1}{\sqrt{3}}(|gf\rangle + |ee\rangle + |fg\rangle), \quad (6)$$

up to local phases. The local ef -frame corrections applied before reporting the density matrix are 0.911 rad on node A and -2.035 rad on node B. Additional tomography phase diagnostics and robustness checks are shown in Supplementary Figs. S10 and S11.

E. Qutrit tomography and readout correction

Qutrit state tomography is performed by applying a tomographically complete set of analysis rotations before three-state readout [26, 56, 57]. For a single qutrit, we use nine analysis settings that map the populations and the real and imaginary parts of the $|g\rangle$ - $|e\rangle$, $|g\rangle$ - $|f\rangle$ and $|e\rangle$ - $|f\rangle$ coherences onto measured three-level populations. For two-qutrit tomography, the same single-qutrit analysis set is applied independently to both nodes, giving 9×9 joint analysis settings and nine three-state joint readout outcomes for each setting. In the main tomography datasets, each probability for a given analysis setting is obtained from 4000 single-shot repetitions. The explicit analysis rotations are listed in the Supplementary Information.

For each measured qutrit, the readout assignment matrix M is independently calibrated, with elements $M_{ij} = P(\text{measured } i | \text{prepared } j)$. For two-qutrit tomography, the full readout matrix is taken as the tensor product of the independently calibrated single-qutrit assignment matrices. The measured probability vector p_{meas} is corrected by

$$p_{\text{corr}} = M^{-1} p_{\text{meas}}. \quad (7)$$

The density matrix is then obtained from the corrected tomography probabilities by maximum-likelihood estimation with unit-trace and positive-semidefinite constraints. The readout matrices used for the data in Figs. 3 and 4 are shown in Supplementary Fig. S8. Unless otherwise specified, the fidelities and density matrices reported

in the main text are readout corrected.

F. Process tomography and benchmark definitions

For qutrit process tomography, we prepare nine linearly independent qutrit input states on node A, transfer each state through the microwave link, and reconstruct the corresponding output density matrix on node B with qutrit state tomography. The input set is generated from $|g\rangle$ by calibrated rotations in the ge and ef subspaces, and spans the three populations and the three pairwise coherences of the qutrit. The same analysis is applied to the input states in separate calibration runs to account for state-preparation imperfections. The input-output density-matrix pairs are then used to infer the process matrix χ in the Gell-Mann basis [52, 53]. The process fidelity is calculated as

$$F_\chi = \text{Tr}(\chi_{\text{exp}} \chi_{\text{ideal}}), \quad (8)$$

with both process matrices represented in the same basis and normalization convention. The transferred-state fidelity is calculated between the reconstructed output state and the corresponding ideal target state. The mean state fidelity is the average over the tested input states.

The classical qutrit benchmark used for state transfer is $F_{\text{cl}} = 1/2$, corresponding to the optimal measure-and-prepare strategy for an unknown qutrit state [34]. The qubit-channel benchmark is $F_{\text{qb}} = 3/4$, the maximum average fidelity for transmitting an arbitrary qutrit through an effective two-dimensional quantum channel [35]. These bounds are used only for the full qutrit-transfer channel, not for the primitive two-level transfer processes.

G. Entanglement metrics and dense-coding capacity

The two-qutrit state fidelity is calculated with respect to $|\Psi_{\text{qutrit}}\rangle$ using the standard state-fidelity convention [58]. The negativity is computed from the partial transpose of the reconstructed density matrix [37, 38],

$$\mathcal{N}(\rho) = \frac{\|\rho^{T_B}\|_1 - 1}{2}. \quad (9)$$

For a maximally entangled qutrit target, any state with Schmidt number at most two has fidelity no larger than $2/3$ [36]. For any two-qubit state, the maximum negativity is 0.5; values above this limit certify entanglement that cannot be represented within a two-qubit Hilbert space.

The dense-coding capacity is evaluated from the reconstructed two-qutrit state as [3–5]

$$C = \log_2 d + S(\rho_B) - S(\rho_{AB}), \quad (10)$$

with local dimension $d = 3$, reduced state $\rho_B = \text{Tr}_A(\rho_{AB})$, and von Neumann entropy $S(\rho) = -\text{Tr}(\rho \log_2 \rho)$. We compare this value with the classical qutrit value $\log_2 3$ and the ideal qubit dense-coding limit of 2 bits. The CGLMP parameter I_3 is calculated from the reconstructed density matrix using the standard two-setting, three-outcome measurement bases [6]. The full convention and basis mapping are provided in the Supplementary Information.

H. Cascaded master-equation simulation

The simulations use a pulse-level cascaded master equation implemented in QuTiP [48–51]. The model includes the qutrit degrees of freedom of both nodes, the auxiliary resonator modes, the directional coupling between the two nodes, internal resonator loss, channel transmission efficiency and qutrit relaxation. The channel efficiency and internal-loss parameters used for the main figures are

$$\begin{aligned} \eta_c &= 0.92, \\ \kappa_{\text{int},A}/2\pi &= 0.0208 \text{ MHz}, \quad \kappa_{\text{int},B}/2\pi = 0.0176 \text{ MHz}. \end{aligned} \quad (11)$$

Dephasing is included as a T_1 -corrected quasi-static $1/f$ -like detuning ensemble. For each noise realization, the qutrit transition frequencies are shifted by static detunings drawn from Gaussian distributions whose widths are extracted from Ramsey measurements after subtracting the contribution from energy relaxation. The simulated density matrices and populations are averaged over the detuning ensemble. This treatment captures the slow dephasing that dominates the experiment without overestimating the loss of coherence during the 200 ns transfer pulses. The model uses fixed calibrated parameters during each tomography simulation and does not include additional drift of the transfer resonance or readout assignment matrix. The detailed Hamiltonian, collapse operators, noise extraction, $1/f$ -versus-Markovian noise comparison and sine-versus-sech pulse comparison are given in the Supplementary Information.

I. Uncertainties

Error bars in the population-dynamics data are obtained from repeated measurements and grouped dataset averages. Error bars for state and process fidelities are calculated from repeated tomography reconstructions. For the Purcell-filter linewidth calibration, the uncertainty in T_{cav} is taken from the covariance matrix of the single-exponential fit and propagated to $\kappa/2\pi$ using

$$\delta(\kappa/2\pi) = \frac{\delta T_{\text{cav}}}{2\pi T_{\text{cav}}^2}. \quad (12)$$

SUPPLEMENTARY INFORMATION

Supplementary Information accompanies this manuscript. It includes the sample layout, measurement-chain schematic, device parameters and readout matrices, cavity spectroscopy, Purcell-filter linewidth calibration, chirped-pulse calibration, primitive transfer delay and phase scans, primitive tomography diagnostics, tomography phase diagnostics, readout-correction checks, the cascaded master-equation derivation, the $1/f$ -dephasing model, the dense-coding and CGLMP conventions, the waveform comparison, the inverse-designed REG waveform construction, and the simulation error budget.

DATA AVAILABILITY STATEMENT

The data produced in this work is available from the corresponding authors upon reasonable request.

ACKNOWLEDGMENTS

The authors thank Prof. Duanlu Zhou for insightful discussions. This work was supported by the Micro/Nano Fabrication Laboratory of Synergetic Extreme Condition User Facility (SECUF). Devices were made at the Nanofabrication Facilities at the Institute of Physics, CAS in Beijing. The authors thank Beijing Naishu Electronics Co., Ltd. for providing support of RF-DAC and RF-ADC based on RFSoc FPGA. This work was supported by: Innovation Program for Quantum Science and Technology (Grant No. 2021ZD0301800), the National Natural Science Foundation of China (Grants No. 12574540, 92265207, T2121001, 12204528)

AUTHOR CONTRIBUTIONS

D.-N.Z., H.F and X.L. supervised the project. X.L. conceived the idea. X.L., Y.-J.L and Z.-Y.M designed the sample. X.L. performed the experiment, processed the data and wrote this manuscript. Z.-Y.M fabricated the sample. Y.H. and S.-L.Z helped with several iterations of the sample. All authors contributed to the discussions and production of the manuscript.

COMPETING INTERESTS

The authors declare no competing interests.

-
- [1] Kimble, H. J. The quantum internet. *Nature* **453**, 1023–1030 (2008).
- [2] Wehner, S., Elkouss, D. & Hanson, R. Quantum internet: A vision for the road ahead. *Science* **362**, eaam9288 (2018).
- [3] Bennett, C. H. & Wiesner, S. J. Communication via one- and two-particle operators on Einstein-Podolsky-Rosen states. *Physical Review Letters* **69**, 2881–2884 (1992).
- [4] Horodecki, M., Horodecki, P., Horodecki, R., Leung, D. W. & Terhal, B. M. Classical capacity of a noiseless quantum channel assisted by noisy entanglement. *Quantum Information and Computation* **1**, 70–78 (2001).
- [5] Bowen, G. Classical information capacity of superdense coding. *Physical Review A* **63**, 022302 (2001).
- [6] Collins, D., Gisin, N., Linden, N., Massar, S. & Popescu, S. Bell inequalities for arbitrarily high-dimensional systems. *Physical Review Letters* **88**, 040404 (2002).
- [7] Erhard, M., Krenn, M. & Zeilinger, A. Advances in high-dimensional quantum entanglement. *Nature Reviews Physics* **2**, 365–381 (2020).
- [8] Mair, A., Vaziri, A., Weihs, G. & Zeilinger, A. Entanglement of the orbital angular momentum states of photons. *Nature* **412**, 313–316 (2001).
- [9] Vaziri, A., Weihs, G. & Zeilinger, A. Experimental two-photon, three-dimensional entanglement for quantum communication. *Physical Review Letters* **89**, 240401 (2002).
- [10] Cerf, N. J., Bourennane, M., Karlsson, A. & Gisin, N. Security of quantum key distribution using d -level systems. *Physical Review Letters* **88**, 127902 (2002).
- [11] Kues, M. *et al.* On-chip generation of high-dimensional entangled quantum states and their coherent control. *Nature* **546**, 622–626 (2017).
- [12] Ringbauer, M. *et al.* A universal qudit quantum processor with trapped ions. *Nature Physics* **18**, 1053–1057 (2022).
- [13] Hrmo, P. *et al.* Native qudit entanglement in a trapped ion quantum processor. *Nature Communications* **14**, 2242 (2023).
- [14] Fu, Y. *et al.* Experimental investigation of quantum correlations in a two-qutrit spin system. *Physical Review Letters* **129**, 100501 (2022).
- [15] Storz, S. *et al.* Loophole-free bell inequality violation with superconducting circuits. *Nature* **617**, 265–270 (2023).
- [16] Kulikov, A. *et al.* Device-independent randomness amplification. *Nature* (2026).
- [17] Blais, A., Grimsmo, A. L., Girvin, S. M. & Wallraff, A. Circuit quantum electrodynamics. *Reviews of Modern Physics* **93**, 025005 (2021).
- [18] Pechal, M. *et al.* Microwave-controlled generation of shaped single photons in circuit quantum electrodynamics. *Physical Review X* **4**, 041010 (2014).
- [19] Wenner, J. *et al.* Catching time-reversed microwave coherent state photons with 99.4% absorption efficiency. *Physical Review Letters* **112**, 210501 (2014).
- [20] Kurpiers, P. *et al.* Deterministic quantum state transfer and remote entanglement using microwave photons. *Nature* **558**, 264–267 (2018).
- [21] Axline, C. J. *et al.* On-demand quantum state transfer and entanglement between remote microwave cavity memories. *Nature Physics* **14**, 705–710 (2018).
- [22] Magnard, P. *et al.* Microwave quantum link between superconducting circuits housed in spatially separated cryogenic systems. *Physical Review Letters* **125**, 260502 (2020).
- [23] Burkhardt, L. D. *et al.* Error-detected state transfer and entanglement in a superconducting quantum network. *PRX Quantum* **2**, 030321 (2021).
- [24] Zhong, Y. *et al.* Deterministic multi-qubit entanglement in a quantum network. *Nature* **590**, 571–575 (2021).
- [25] Neeley, M. *et al.* Emulation of a quantum spin with a superconducting phase qudit. *Science* **325**, 722–725 (2009).
- [26] Bianchetti, R. *et al.* Control and tomography of a three level superconducting artificial atom. *Physical Review Letters* **105**, 223601 (2010).
- [27] Xu, H. K. *et al.* Coherent population transfer between uncoupled or weakly coupled states in ladder-type superconducting qutrits. *Nature Communications* **7**, 11018 (2016).
- [28] Morvan, A. *et al.* Qutrit randomized benchmarking. *Physical Review Letters* **126**, 210504 (2021).
- [29] Goss, N. *et al.* High-fidelity qutrit entangling gates for superconducting circuits. *Nature Communications* **13**, 7481 (2022).
- [30] Brown, T. *et al.* Trade off-free entanglement stabilization in a superconducting qutrit-qubit system. *Nature Communications* **13**, 3994 (2022).
- [31] Kurpiers, P. *Quantum Networks with Superconducting Circuits*. Ph.D. thesis, ETH Zurich (2019).
- [32] Li, X. *et al.* On-demand shaped-photon emission based on a parametrically modulated qubit. *Physical Review Applied* **23**, 024019 (2025).
- [33] Magnard, P. *et al.* Fast and unconditional all-microwave reset of a superconducting qubit. *Phys. Rev. Lett.* **121**, 060502 (2018).
- [34] Massar, S. & Popescu, S. Optimal extraction of information from finite quantum ensembles. *Physical Review Letters* **74**, 1259–1263 (1995).
- [35] Horodecki, M., Horodecki, P. & Horodecki, R. General teleportation channel, singlet fraction, and quasidistillation. *Physical Review A* **60**, 1888–1898 (1999).
- [36] Terhal, B. M. & Horodecki, P. Schmidt number for density matrices. *Physical Review A* **61**, 040301 (2000).
- [37] Peres, A. Separability criterion for density matrices. *Physical Review Letters* **77**, 1413–1415 (1996).
- [38] Vidal, G. & Werner, R. F. Computable measure of entanglement. *Physical Review A* **65**, 032314 (2002).
- [39] Horodecki, R., Horodecki, P., Horodecki, M. & Horodecki, K. Quantum entanglement. *Reviews of Modern Physics* **81**, 865–942 (2009).
- [40] Koch, J. *et al.* Charge-insensitive qubit design derived from the cooper pair box. *Physical Review A* **76**, 042319 (2007).
- [41] Houck, A. *et al.* Controlling the spontaneous emission of a superconducting transmon qubit. *Physical review letters* **101**, 080502 (2008).
- [42] Reed, M. D. *et al.* Fast reset and suppressing spontaneous emission of a superconducting qubit. *Applied Physics Letters* **96** (2010).
- [43] Yan, H. *et al.* Broadband bandpass purcell filter for circuit quantum electrodynamics. *Applied Physics Letters* **123**, 134001 (2023).

- [44] Didier, N., Sete, E. A., da Silva, M. P. & Rigetti, C. Analytical modeling of parametrically modulated transmon qubits. *Physical Review A* **97**, 022330 (2018).
- [45] Cirac, J. I., Zoller, P., Kimble, H. J. & Mabuchi, H. Quantum state transfer and entanglement distribution among distant nodes in a quantum network. *Physical Review Letters* **78**, 3221 (1997).
- [46] Yao, W., Liu, R.-B. & Sham, L. Theory of control of the spin-photon interface for quantum networks. *Physical review letters* **95**, 030504 (2005).
- [47] Korotkov, A. N. Flying microwave qubits with nearly perfect transfer efficiency. *Physical Review B* **84**, 014510 (2011).
- [48] Gardiner, C. W. Driving a quantum system with the output field from another driven quantum system. *Physical Review Letters* **70**, 2269–2272 (1993).
- [49] Carmichael, H. J. Quantum trajectory theory for cascaded open systems. *Physical Review Letters* **70**, 2273–2276 (1993).
- [50] Johansson, J., Nation, P. & Nori, F. Qutip: An open-source python framework for the dynamics of open quantum systems. *Computer Physics Communications* **183**, 1760–1772 (2012).
- [51] Johansson, J., Nation, P. & Nori, F. Qutip 2: A python framework for the dynamics of open quantum systems. *Computer Physics Communications* **184**, 1234–1240 (2013).
- [52] Poyatos, J., Cirac, J. I. & Zoller, P. Complete characterization of a quantum process: the two-bit quantum gate. *Physical Review Letters* **78**, 390 (1997).
- [53] Chuang, I. L. & Nielsen, M. A. Prescription for experimental determination of the dynamics of a quantum black box. *Journal of Modern Optics* **44**, 2455–2467 (1997).
- [54] Nielsen, M. A. & Chuang, I. L. *Quantum computation and quantum information* (Cambridge university press, 2010).
- [55] Miyamura, T. *et al.* Generation of frequency-tunable shaped single microwave photons using a fixed-frequency superconducting qubit. *PRX Quantum* **6**, 020347 (2025).
- [56] Steffen, M. *et al.* Measurement of the entanglement of two superconducting qubits via state tomography. *Science* **313**, 1423–1425 (2006).
- [57] Neeley, M. *et al.* Process tomography of quantum memory in a josephson-phase qubit coupled to a two-level state. *Nature Physics* **4**, 523–526 (2008).
- [58] Jozsa, R. Fidelity for mixed quantum states. *Journal of modern optics* **41**, 2315–2323 (1994).

Supplementary Information for “A superconducting qutrit link beyond the qubit limit”

Xiang Li,^{1,2,3,*} Zheng-Yang Mei,^{1,2} Yang He,^{1,2} Si-Lu Zhao,^{1,2} Yan-Jun Liu,^{1,2} Xiao-Hui Song,^{1,4} Kai Xu,^{1,4,5} Zhong-Cheng Xiang,^{1,4} Dong-Ning Zheng,^{1,2,4,†} and Heng Fan^{1,2,4,5,‡}

¹*Beijing National Laboratory for Condensed Matter Physics,
Institute of Physics, Chinese Academy of Sciences, Beijing 100190, China*

²*School of Physical Sciences, University of Chinese
Academy of Sciences, Beijing 100049, China*

³*Centre for Quantum Technologies,
National University of Singapore, 117543, Singapore*

⁴*Hefei National Laboratory, Hefei 230088, China*

⁵*Beijing Academy of Quantum Information Sciences, Beijing 100193, China*

(Dated: June 30, 2026)

* francis_li@nus.edu.sg

† dzheng@iphy.ac.cn

‡ hfan@iphy.ac.cn

CONTENTS

I. DEVICE, WIRING AND MATCHED PHOTON INTERFACE	3
A. Sample layout and node architecture	3
B. Cryogenic wiring and measurement setup	4
C. Device parameters and operating points	6
D. Device coherence, readout calibration, and simulation inputs	7
E. Cavity spectroscopy and tunable matching of the two nodes	9
F. Tunable Purcell-filter control of the transmission-resonator linewidth	11
G. Chirped-pulse calibration for the transfer primitives	12
II. TRANSFER PRIMITIVES AND TOMOGRAPHY RECONSTRUCTION	15
A. Primitive delay and phase calibrations	15
B. Logical state maps for qutrit transfer and REG	17
C. Tomography measurement bases and readout correction	18
D. Primitive transfer and REG QST diagnostics	21
E. Phase and matrix-distance diagnostics	21
III. BEYOND-QUBIT BENCHMARKS AND ROBUSTNESS CHECKS	25
A. Metric definitions and readout-correction confidence	25
IV. PULSE-LEVEL SIMULATION, DEPHASING MODEL AND ERROR BUDGET	29
A. Cascaded master-equation model and dephasing implementation	29
B. Sine and sech waveform comparison	33
C. Full-model inverse design of REG waveforms	37
D. Simulation error budget for qutrit transfer and REG	41
References	44

Supplementary roadmap. The table below summarizes how the Supplementary Information supports the main-text claims and figures.

Main-text claim or figure	Supporting Supplementary material and key diagnostics
Matched qutrit-link architecture and photon interface, Fig. 1	Sec. I and Figs. S1–S6: device layout, wiring, operating points, frequency matching, tunable linewidth calibration and chirped-pulse calibration.
Primitive transfer and arbitrary qutrit-state transfer, Figs. 2 and 3	Sec. II, Figs. S7–S10 and Table S2: delay and phase calibration, logical state maps, tomography bases, independently calibrated readout correction, imaginary components and matrix-distance diagnostics.
Remote qutrit entanglement and beyond-qubit benchmarks, Fig. 4	Sec. III and Fig. S11: metric definitions, readout-correction sensitivity, assignment-matrix resampling and repetition-level confidence checks for fidelity, negativity, dense-coding capacity and I_3 .
Pulse-level simulation, waveform modelling and improvement priorities	Sec. IV, Figs. S12–S14 and Tables S3–S5: cascaded master-equation model, quasi-static dephasing implementation, sine/sech waveform comparison, inverse-designed REG waveform construction and cumulative error budget.

I. DEVICE, WIRING AND MATCHED PHOTON INTERFACE

A. Sample layout and node architecture

Figure S1 shows the physical implementation of the two-node link. Each node contains a flux-tunable asymmetric-junction transmon used as a qutrit, a transmission resonator used for photon emission and capture, a readout resonator with a Purcell filter, and a tunable Purcell-filter interface to the microwave link. The tunable interface is connected to the bonding pad through a half-wavelength impedance transformer. This transformer places a distributed-current node near the wire-bond position, reducing Joule heating and suppressing additional loss introduced by the wire bonds in the inter-node link. The chip is enclosed in a gold-plated copper box with an aluminium lid, and indium seals are used

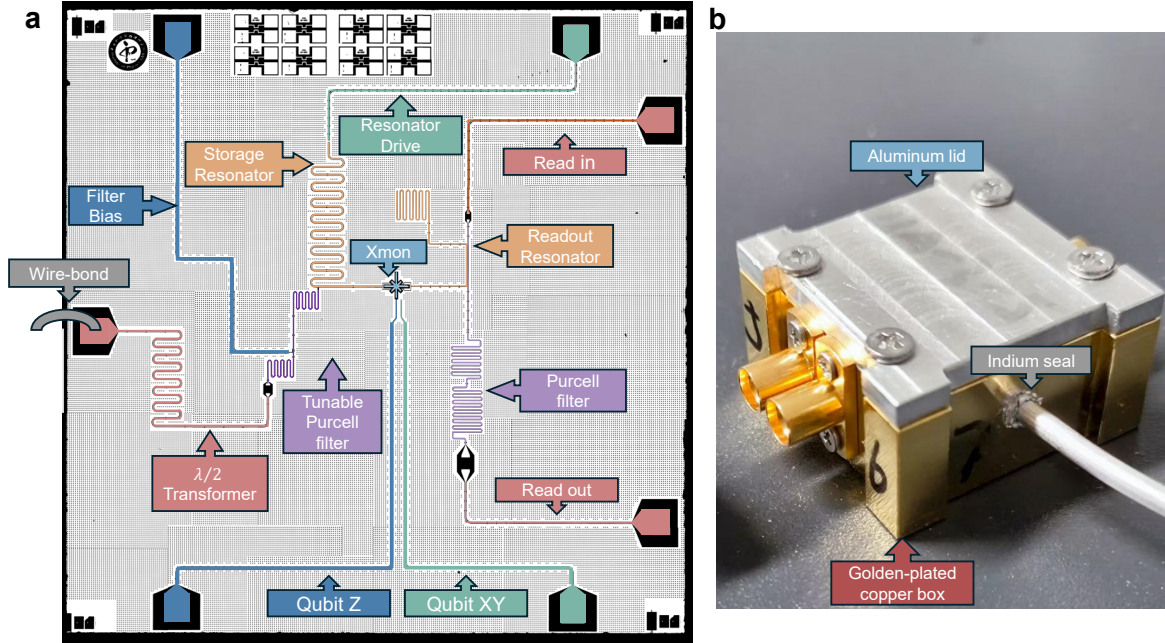


FIG. S1: **Sample layout and packaged two-node device.** (a) Device structure of one superconducting qutrit node. Each node contains a flux-tunable asymmetric-junction transmon, a transmission resonator used for photon emission and capture, a readout resonator with its own Purcell filter, and a tunable Purcell-filter interface to the microwave link. (b) Packaged sample box after assembly. The package uses an aluminium lid, a gold-plated copper box and indium seals around the aluminium coaxial-cable ports to shield the chip from residual free-space infrared radiation inside the dilution refrigerator. The two independently packaged nodes are connected by the directional microwave link used for cascaded state transfer and remote entanglement generation.

around the aluminium coaxial-cable ports. This package reduces direct infrared exposure of the chip to residual free-space radiation in the dilution refrigerator. The two chips are mounted in independent sample boxes and connected through a directional microwave link.

B. Cryogenic wiring and measurement setup

Figure S2 summarizes the wiring and control stack used for the experiment. The samples are mounted at the mixing-chamber stage of a Bluefors dilution refrigerator. The microwave input lines contain cryogenic attenuation and infrared/low-pass filtering before reaching the sample boxes. The total attenuation is 39 dB on both the qutrit flux-control (Z) lines

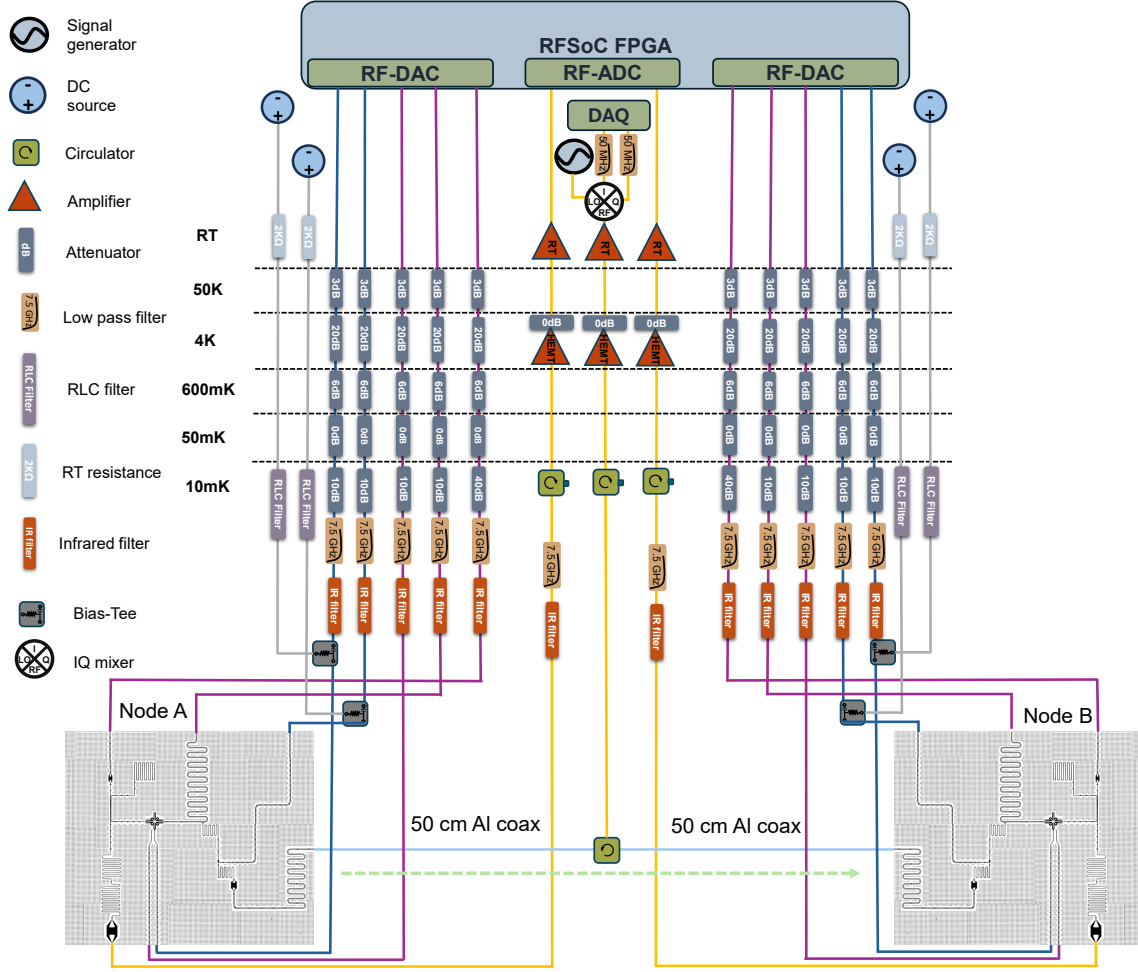


FIG. S2: **Cryogenic wiring and room-temperature control setup.** The diagram shows the cryogenic wiring, room-temperature microwave-control and digitization chain, and the directional cascaded-channel layout used for photon emission from node A and capture by node B. It includes the input attenuation and filtering, qubit microwave-control lines, qutrit flux-modulation lines, Purcell-filter z -control lines, storage-resonator drive lines, readout lines, circulators/isolators, amplification chain, RFSoc/RF-DAC/RF-ADC hardware, mixers, local oscillators, and the one-metre inter-node link.

and the microwave-control (XY) lines, and 69 dB on the readout input line. Local qutrit rotations are applied through the qubit microwave-control lines. The $e0g1$ primitive is driven through the qutrit flux-modulation line, while the $f0g1$ Raman pulse is applied through the microwave-control chain. Compared with the setup used in our earlier shaped-photon experiment [1], each node also includes an additional Purcell-filter z -control line, which tunes the coupling between the transmission resonator and the waveguide. The storage-resonator

drive lines are wired for resonator characterization and future direct resonator operations; they are not used in the qutrit-link pulse sequences analyzed in the main text.

The room-temperature electronics follow the same RFSoc-based architecture as in our previous photon-shaping experiment [1]. The control pulses are generated by RF-DAC channels implemented on Xilinx Zynq UltraScale+ RFSoc XCZU47DR boards, operated at a sampling rate of 8.0 GSa/s. These channels generate the qutrit-control pulses, readout pulses, flux-parametric modulation pulses, Raman pulses and Purcell-filter z -pulses, with additional room-temperature filtering, amplification and IQ mixing used where required by the frequency band. The readout signals are routed through separate readout lines with cryogenic non-reciprocal elements and a low-noise amplification chain before room-temperature demodulation and digitization by RF-ADC channels based on Xilinx Zynq UltraScale+ RFSoc XCZU47DR boards operated at 4.0 GSa/s. Local oscillators and the RFSoc clocks are referenced to a rubidium frequency standard (Stanford Research Systems FS725), providing phase-coherent up-conversion, down-conversion and digitization during each acquisition block. The photon-transfer path is directional and separate from the readout chains: photons emitted from the transmission resonator of node A propagate through the one-metre inter-node link and are captured by the matched transmission resonator of node B. The microwave and flux-control channels are synchronized by the room-temperature control electronics. The calibrated relative delays reported in the main text and in Fig. S7 therefore include both microwave propagation through the link and fixed cable/electronics delays.

C. Device parameters and operating points

Table S1 collects the operating-point parameters used in the main experiment and the cascaded-master-equation simulations. The purpose of the table is to make clear which quantities are independently calibrated before the qutrit-link benchmarks are evaluated. The values of T_1 , T_ϕ , η_c , and $\kappa_{\text{int}}/2\pi$ are the values used in the current simulations. The measured loaded linewidths are the nearest directly measured high-bandwidth values to 10 MHz, rather than interpolated ideal values.

The thermal populations are the independently calibrated residual excited-state populations at the operating point. The local qutrit control pulses use 20 ns calibrated π rotations on both nodes, and the readout integration time is 0.5 μs . The photon-mediated transfer

TABLE S1: **Device parameters and operating points.** The table lists independently calibrated operating-point parameters used in the qutrit-link experiment and in the pulse-level simulations.

Parameter	Node A	Node B
Qutrit transition frequency $\omega_{ge}/2\pi$	6131.1 MHz	6131.8 MHz
Qutrit transition frequency $\omega_{ef}/2\pi$	5921.4 MHz	5922.6 MHz
Anharmonicity $\alpha/2\pi$	-209.8 MHz	-209.1 MHz
Auxiliary-resonator frequency $\omega_{\text{aux}}/2\pi$	7.4347 GHz	7.4347 GHz
Readout-resonator frequency $\omega_r/2\pi$	4.7065 GHz	4.7065 GHz
Readout integration length	0.5 μs	0.5 μs
Local qutrit π -pulse length	20 ns	20 ns
Thermal population	$1.50 \pm 0.14\%$	$1.57 \pm 0.04\%$
Measured loaded linewidth $\kappa/2\pi$	10.72 MHz	10.28 MHz
Internal loss rate $\kappa_{\text{int}}/2\pi$	0.0208 MHz	0.0176 MHz
$T_{1,ge}$	21.78 μs	22.16 μs
$T_{1,ef}$	9.79 μs	9.75 μs
$T_{\phi,ge}$	3.80 μs	2.20 μs
$T_{\phi,ef}$	3.75 μs	2.20 μs
Channel efficiency η_c	0.92	

primitives use chirped 200 ns sine envelopes.

D. Device coherence, readout calibration, and simulation inputs

Figure S3 collects the device parameters that enter the tomography and simulation. Both nodes use asymmetric-junction transmons, so the operating flux biases are chosen for interface matching rather than for identical transmon frequencies. At these biases, the $|g\rangle \leftrightarrow |e\rangle$ relaxation times are $T_{1,ge} = 21.78 \mu\text{s}$ for node A and $22.16 \mu\text{s}$ for node B. The $|e\rangle \leftrightarrow |f\rangle$ transition relaxes faster, with $T_{1,ef} = 9.79 \mu\text{s}$ and $9.75 \mu\text{s}$, respectively. We use these measured values directly as energy-relaxation collapse rates in the cascaded master-equation model.

The Ramsey envelopes decay faster than energy relaxation alone. We attribute the re-

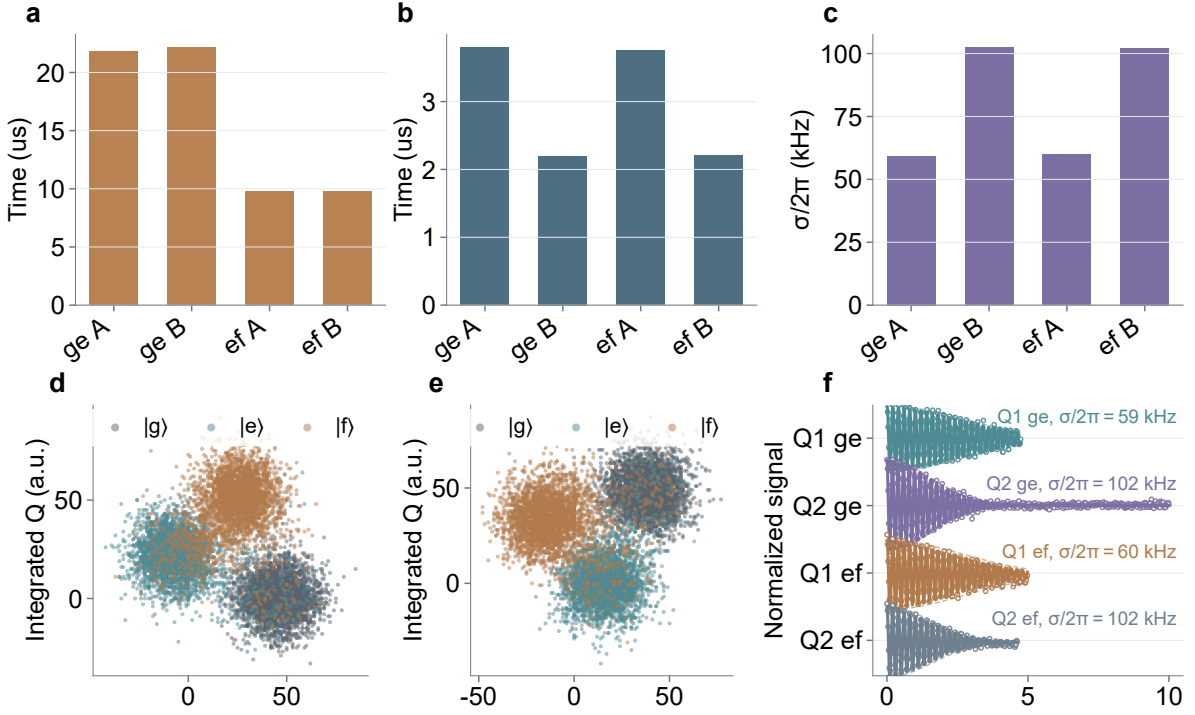


FIG. S3: **Device coherence, qutrit readout calibration, and simulation inputs.**

(a) Energy-relaxation times T_1 for the ge and ef transitions of the two nodes. (b) Ramsey-derived pure-dephasing times T_ϕ after subtracting the relaxation-limited contribution. (c) Corresponding quasi-static detuning-noise widths $\sigma/2\pi$ used in the $1/f$ -like dephasing ensemble. (d,e) Representative three-state IQ readout clouds for node A and node B, showing separation of the $|g\rangle$, $|e\rangle$, and $|f\rangle$ states. (f) T_1 -corrected Ramsey fits used to extract the quasi-static detuning-noise widths; dashed curves indicate the Gaussian envelope produced by the quasi-static $1/f$ -like detuning-noise model.

maining decay to low-frequency, $1/f$ -like detuning noise and treat it in the quasi-static limit. Each Ramsey trace is fitted with

$$P(t) = y_0 + A \exp \left[-\Gamma_{\text{rad}} t - \frac{(\sigma t)^2}{2} \right] \cos(2\pi f t + \phi), \quad (\text{S1})$$

where Γ_{rad} is fixed by the measured T_1 values. For a ge coherence,

$$\Gamma_{\text{rad},ge} = \frac{1}{2T_{1,ge}}, \quad (\text{S2})$$

whereas for an ef coherence,

$$\Gamma_{\text{rad},ef} = \frac{1}{2} \left(\frac{1}{T_{1,ge}} + \frac{1}{T_{1,ef}} \right). \quad (\text{S3})$$

After the T_1 contribution is fixed, the Gaussian part of the envelope defines the rms quasi-static detuning width σ . This form gives a better description of the measured Ramsey traces than a single Markovian exponential decay and is the dephasing model used in the main simulations. The extracted widths are $\sigma_{ge,A}/2\pi = 59.24$ kHz, $\sigma_{ge,B}/2\pi = 102.47$ kHz, $\sigma_{ef,A}/2\pi = 60.01$ kHz, and $\sigma_{ef,B}/2\pi = 102.18$ kHz, corresponding to $T_\phi = \sqrt{2}/\sigma$ values of $3.80 \mu\text{s}$, $2.20 \mu\text{s}$, $3.75 \mu\text{s}$, and $2.20 \mu\text{s}$.

The IQ-cloud measurements in Fig. S3(d,e) show that the three qutrit levels are resolved by the heterodyne readout chain. The assignment matrices used to correct tomography probabilities are shown separately in Fig. S8, where the full two-qutrit correction matrices are also displayed.

E. Cavity spectroscopy and tunable matching of the two nodes

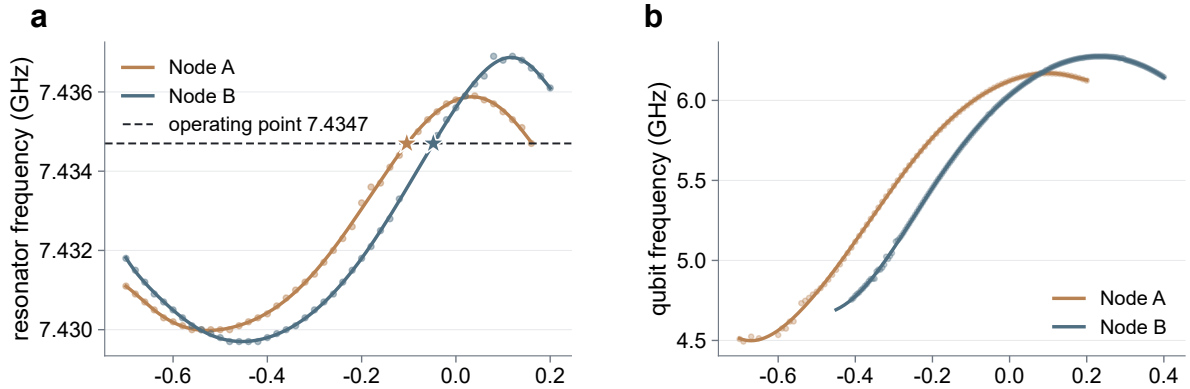


FIG. S4: **Cavity spectroscopy and tunable matching of the two remote interfaces.** (a) Smoothed transmission-resonator frequency trajectories extracted from background-corrected spectroscopy maps using branch-dependent extrema and a higher-order Chebyshev guide. The dashed line marks the matched operating frequency near 7.4347 GHz, and stars mark the negative-bias operating points used in the experiment. (b) Qubit spectroscopy trajectories extracted from the corresponding transmon spectroscopy maps, showing the large flux-tuning range of the asymmetric-junction transmons.

The cavity spectroscopy in Fig. S4 is used to choose the two remote interface frequencies. Each auxiliary resonator is dispersively shifted by its transmon, whose asymmetric SQUID

loop provides a tuning range on the order of 2 GHz. The qutrit flux bias therefore moves the effective auxiliary-resonator frequency, while the Purcell-filter bias controls the coupling rate to the waveguide. These two controls are calibrated separately before the state-transfer experiment.

In the cascaded transfer picture, the photon must be matched twice: its carrier frequency must be resonant with the receiver interface, and its temporal envelope must match the receiver’s time-dependent absorption mode. Frequency matching fixes the carrier; linewidth matching fixes the bandwidth scale of the emitted and absorbed wave packets. Both are needed before the pulse-shape calibration can be meaningful.

The transmission-resonator spectroscopy maps are background-corrected line by line before ridge extraction because the raw background varies with qubit flux bias. This correction is used only for visualization and ridge extraction; it does not change the measured operating frequency. Because the contrast of the resonator-like feature changes in different flux regions, the ridge is extracted with a branch-dependent criterion: for node A, the response maximum is used from flux 0.15 to -0.2 , while the response minimum is used from -0.2 to -0.7 ; for node B, the response maximum is used from flux 0.1 to -0.05 , while the response minimum is used outside this interval. A few node-B points in the contrast-changing region are discarded when they jump discontinuously from the neighbouring resonator branch. The remaining points are connected by a tenth-order Chebyshev guide used only for visualization, rather than by an exact interpolant or a global sinusoidal fit, because the dressed resonator pull is not expected to be a perfect sine function over the full flux range. The final operating frequency is determined from matched spectroscopy line cuts and lies near 7.4347 GHz. The two stars in Fig. S4a mark the negative-bias operating points used in the experiment; these points are not at the same transmon flux bias in the two nodes, which is expected because the two transmons and their dispersive shifts are not identical.

The qubit spectroscopy in Fig. S4b is extracted by taking the maximum spectroscopy response in each flux-bias row of the auto-asymmetry scans. It shows that both asymmetric-junction transmons can be tuned over a range of about 2 GHz, large enough to bring the two dressed transmission-resonator frequencies into resonance while keeping the qutrit operating points away from the same nominal flux bias. The corresponding linewidth tunability and matched high-bandwidth operating points are shown in the following section.

F. Tunable Purcell-filter control of the transmission-resonator linewidth

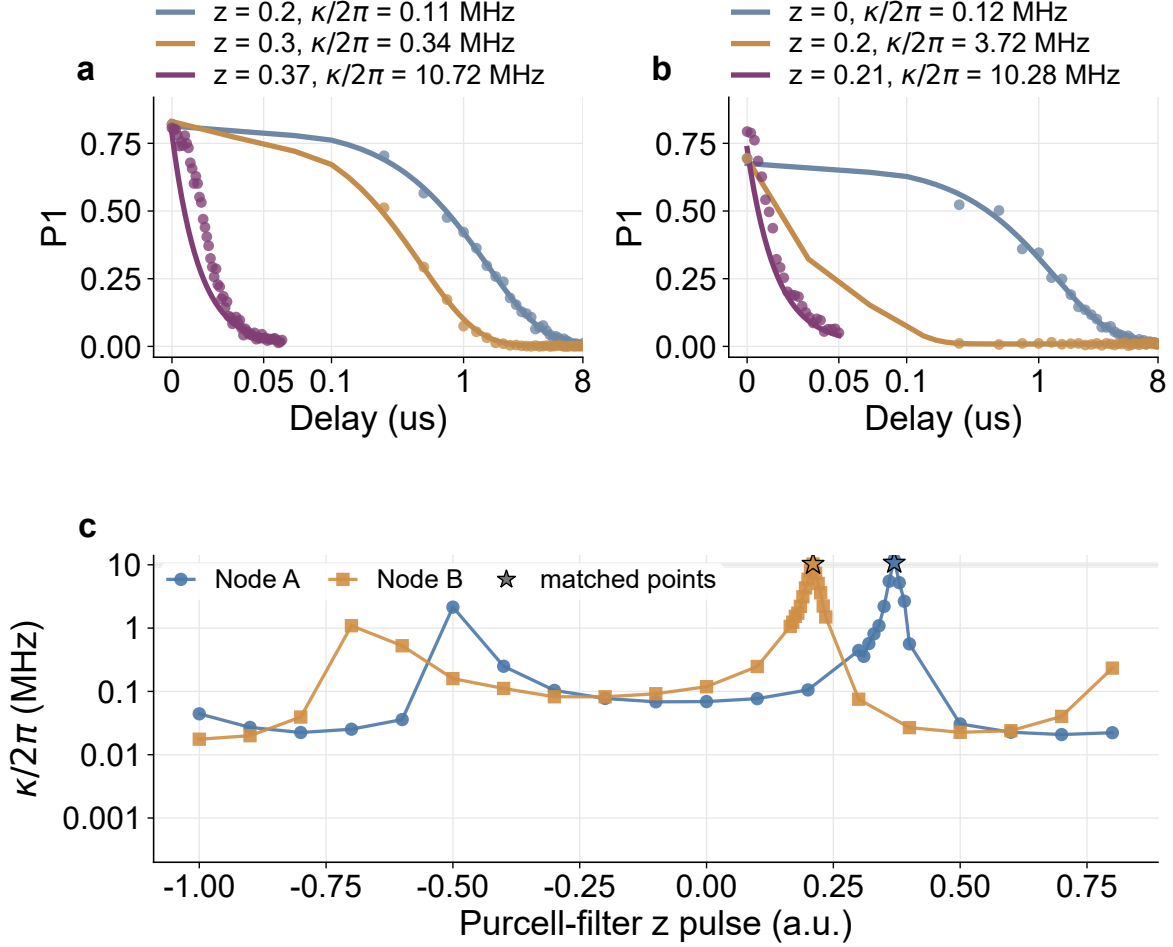


FIG. S5: **Tunable Purcell-filter control of the photon bandwidth.** (a,b) Representative cavity-energy decay measurements for node A and node B at different Purcell-filter control amplitudes. Solid curves are single-exponential fits. (c) Extracted tunable coupling decay rate $\kappa/2\pi = 1/(2\pi T_{\text{cav}})$ as a function of the Purcell-filter z -pulse amplitude. Stars mark the nearest directly measured high-bandwidth settings used to tune the two remote interfaces to comparable photon bandwidths.

In addition to frequency matching, the experiment uses tunable Purcell filters to control the coupling between each auxiliary resonator and the common microwave link [2–5]. We calibrate this control by preparing one photon in the auxiliary resonator and measuring its energy decay as a function of the Purcell-filter control amplitude. For each trace, we fit the measured population to $P_1(t) = P_{\text{off}} + A \exp(-t/T_{\text{cav}})$, and define the loaded photon

linewidth as $\kappa/2\pi = 1/(2\pi T_{\text{cav}})$.

The Purcell-filter bias tunes the loaded transmission-resonator linewidth from the 10^{-2} -MHz range to above 10 MHz, as shown in Fig. S5. The nearest directly measured settings to 10 MHz are $\kappa_A/2\pi = 10.72 \pm 0.44$ MHz at $z = 0.37$ and $\kappa_B/2\pi = 10.28 \pm 0.26$ MHz at $z = 0.21$. Over the measured range the linewidth changes from 0.0208 MHz to 12.16 MHz for node A and from 0.0176 MHz to 10.28 MHz for node B, corresponding to an on/off ratio of about 5.8×10^2 .

The high-bandwidth points are practical calibration points, not precision measurements of a static intrinsic linewidth. The decay measurements use nominal square Purcell-filter z -pulses. At the largest coupling settings, the cavity lifetime is only ~ 15 ns, comparable to the rise time, filtering and settling of the control line. The fitted decay therefore includes the response of the Purcell-filter pulse itself. This explains why the points near $z = 0.37$ for node A and $z = 0.21$ for node B do not follow a simple exponential dependence on the programmed amplitude. For the transfer experiment, the relevant outcome is that both interfaces can be biased to comparable photon bandwidths after their carrier frequencies have been matched.

The smallest loaded linewidths in the same calibration provide an estimate of the intrinsic auxiliary-resonator loss used in the simulations. From the longest measured cavity lifetimes, $T_{\text{cav},A} = 7.645 \mu\text{s}$ and $T_{\text{cav},B} = 9.057 \mu\text{s}$, we obtain $\kappa_{\text{int},A}/2\pi = 0.0208$ MHz and $\kappa_{\text{int},B}/2\pi = 0.0176$ MHz, corresponding to collapse rates $0.1308 \mu\text{s}^{-1}$ and $0.1104 \mu\text{s}^{-1}$, respectively. These values are used as fixed internal-loss collapse rates in all pulse-level simulations.

G. Chirped-pulse calibration for the transfer primitives

The transfer pulses used in the experiment have a fixed 200 ns sine amplitude envelope, but their carrier frequencies are not held fixed during the pulse. The reason is the same for both transfer primitives: the interaction that turns on the photon-mediated coupling also shifts the instantaneous resonance condition. For the $e0g1$ primitive, the flux-parametric modulation activates the $|e, 0\rangle \leftrightarrow |g, 1\rangle$ sideband, but the finite modulation amplitude also changes the time-averaged transmon frequency. In the language used in our earlier shaped-photon experiment [1], this produces an amplitude-dependent sideband detuning through the combined dc frequency shift and the small sideband-induced Lamb shift. For the $f0g1$

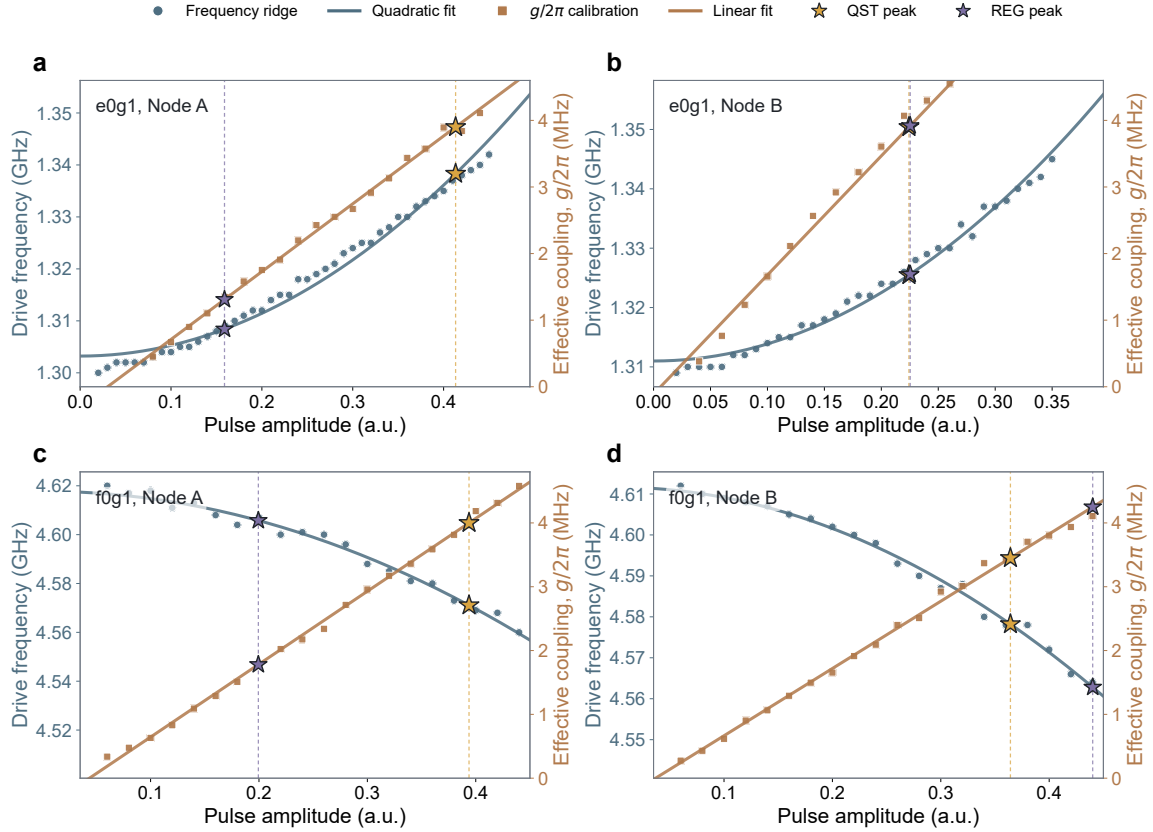


FIG. S6: **Amplitude calibration for the chirped $e0g1$ and $f0g1$ primitives.** (a,b) $e0g1$ calibrations for nodes A and B. (c,d) $f0g1$ calibrations for nodes A and B. Blue circles, read on the left axes, show the extracted resonance frequency from the amplitude–frequency spectroscopy scans; solid blue curves are quadratic fits. Brown squares, read on the right axes, show the independently measured effective coupling $g/2\pi$ extracted from the first $P_{\text{initial}} = 0.5$ crossing of the Rabi traces; solid brown curves are linear fits. Gold and purple stars mark the programmed pulse amplitudes used in the QST and REG experiments. At those amplitudes, the stars on the brown calibration curves give the corresponding effective couplings, while the stars on the blue quadratic fits give the chirped drive frequencies. The dashed vertical guides connect the two calibrations.

primitive, the cavity-assisted Raman drive produces an analogous amplitude-dependent ac Stark shift of the Raman resonance [6–8]. If this detuning were left uncompensated, the beginning, middle and end of the shaped pulse would not be resonant at the same drive frequency. The resulting phase accumulation would distort the emitted photon and reduce the capture efficiency.

We therefore calibrate a dynamic frequency correction for each node and each primitive. For a given primitive $p \in \{e0g1, f0g1\}$, we apply a flat-top calibration pulse with amplitude A , sweep the modulation or Raman-drive frequency, and record the population transfer after the pulse. The resonance appears as a ridge in the two-dimensional maps in Fig. S6. The lowest-amplitude point is excluded from the fit because the transfer contrast is weak and the ridge position is more sensitive to background subtraction. The remaining ridge is fit to

$$\omega_{p,j}(A) = \omega_{p,j}^{(0)} + c_{p,j}A^2, \quad (\text{S4})$$

where $j = A, B$ labels the node. We use a quadratic fit without a linear term because both the average flux-induced frequency shift and the leading ac Stark shift are even in the pulse amplitude. This is also the calibration form used in our previous $e0g1$ shaped-photon work.

During the transfer experiment, the sine envelope $A(t)$ is converted into a time-dependent drive frequency by evaluating the calibrated ridge frequency at the instantaneous pulse amplitude,

$$\omega_d(t) = \omega_{\text{ridge}}[A(t)], \quad (\text{S5})$$

or, equivalently, by programming a time-dependent phase

$$\theta_d(t) = \theta_d(0) + \int_0^t \omega_d(t') dt'. \quad (\text{S6})$$

In the rotating frame of the unchirped drive, this procedure cancels the amplitude-dependent residual detuning $\Delta_p(t) = \omega_{p,j}[A(t)] - \omega_{p,j}^{(0)}$ by adding the opposite time-dependent phase accumulation to the control waveform. The pulse is therefore resonant throughout the full emission or capture window, rather than only at the pulse maximum. In the pulse-level simulation, the transfer coupling $g_{e,j}(t)$ or $g_{f,j}(t)$ is defined in this chirp-corrected resonant frame, while residual detuning noise is included separately through the quasi-static dephasing model described above.

This frequency-ridge calibration is distinct from the amplitude-to-coupling calibration shown on the right axes of Fig. S6. For a fixed chirp-corrected resonance condition, the $e0g1$ flux-modulation amplitude and the $f0g1$ Raman-drive amplitude set the corresponding resonant sideband rates. In the small-amplitude range used for the partial-transfer pulses, the measured transfer rate is linear in the programmed drive amplitude, so the effective peak couplings $g_{e,j}^{\text{max}}$ and $g_{f,j}^{\text{max}}$ used in the simulations are obtained by scaling the calibrated full-transfer couplings. The higher-amplitude full-transfer pulses are calibrated directly from

their transfer oscillations, while the chirp calibration above keeps each instantaneous amplitude resonant during the shaped pulse.

II. TRANSFER PRIMITIVES AND TOMOGRAPHY RECONSTRUCTION

The benchmarks in the main text are obtained from qutrit and two-qutrit tomography. This section therefore separates three logically different ingredients: timing and phase calibrations for the transfer primitives, the fixed readout-assignment correction applied to measured probabilities, and the reconstructed matrices used as diagnostics of the primitive operations. The readout correction is not a state-dependent fit. It is a linear inversion of independently measured assignment matrices, followed by the same tomography reconstruction used for every input state and every repetition.

A. Primitive delay and phase calibrations

The delay and phase scans in Fig. S7 set the timing and phase frame used in the qutrit QPT and REG sequences. For the $e0g1$ delay calibration, node A is prepared by a local π_{ge} pulse, emits through a π_{e0g1} pulse, and node B receives with a delayed π_{e0g1} pulse. For the $f0g1$ delay calibration, node A is prepared by π_{ge} and π_{ef} pulses, emits through a π_{f0g1} pulse, and node B receives with a delayed π_{f0g1} pulse followed by π_{ef} mapping. The Ramsey-type phase calibration scans the receiver analysis pulse $\pi/2_{ge}(\phi)$, compensating the deterministic dynamical phase accumulated during photon propagation and capture. The selected cutoff-time dynamics are shown in the main text, so here we show the calibration scans instead. The Ramsey phase scan in Fig. S7(f) records the readout-corrected receiver population P_{01} as a function of applied phase; the fitted sinusoid defines the virtual- Z reference.

For $e0g1$ transfer, the experiment starts from an excitation in node A and monitors the sender population P_{10} , receiver population P_{01} , and ground-state population P_{00} as the relative timing between the two shaped pulses is varied. The optimal delay is chosen near the maximum of the transferred population and corresponds to the temporal overlap used in the main-text dynamics. For $f0g1$ transfer, the initial excitation is in the second excited state of node A. A final local π_{ef} pulse maps the receiver-side f -state population into the e -state readout manifold, following the experimental sequence. In processing the early-time

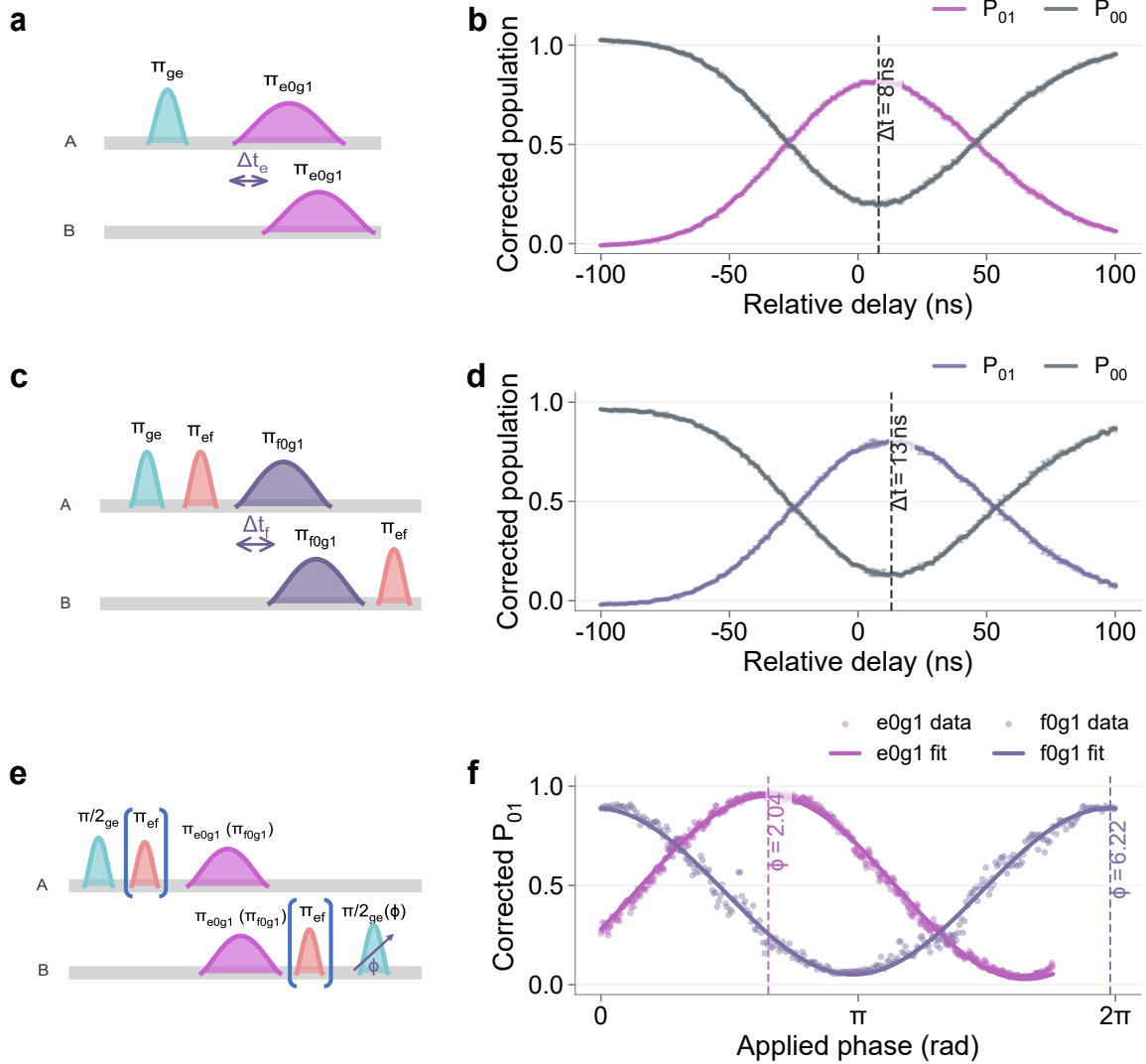


FIG. S7: Primitive delay and phase calibrations for $e0g1$ and $f0g1$ transfer.

(a,c,e) Pulse sequences for the $e0g1$ delay, $f0g1$ delay and Ramsey-type phase calibrations. (b,d) Readout-corrected relative-delay scans for $e0g1$ and $f0g1$, respectively. (f) Ramsey phase scan used to determine the applied phase settings.

$f0g1$ cutoff-time data shown in the main text, P_{10} is added to P_{20} only for the affected early-time region to compensate for a readout-calibration imperfection. The supplementary delay scan is shown as a calibration diagnostic rather than as the final efficiency benchmark.

The solid simulation curves in the corresponding main-text figure are obtained from the same pulse-level cascaded master equation used for the QST, QPT, and REG simulations. The $e0g1$ and $f0g1$ primitive transfer curves are simulated using 200 ns sine pulses, $\eta_c = 0.92$, $\kappa_{\text{int},A}/2\pi = 0.0208$ MHz, $\kappa_{\text{int},B}/2\pi = 0.0176$ MHz, measured T_1 values, and the T_1 -

corrected quasi-static dephasing ensemble. No population trace is shifted separately in this comparison.

B. Logical state maps for qutrit transfer and REG

We spell out the ideal logical maps implemented by the qutrit-transfer and REG pulse sequences. These maps omit deterministic phases from photon propagation, shaped emission and capture, and local qutrit rotations. In the experiment, these phases are absorbed into calibrated drive phases and virtual- Z corrections before tomography.

For qutrit-state transfer, we write $|n_1 n_2\rangle$ for the photon-number state of the first and second temporal modes. The first temporal mode is generated and absorbed by the $f0g1$ primitive, while the second temporal mode is generated and absorbed by the $e0g1$ primitive. The emission stage maps

$$\begin{aligned} (\alpha |g\rangle + \beta |e\rangle + \gamma |f\rangle)_A |g\rangle_B |0_1 0_2\rangle &\xrightarrow{\pi_{f0g1}} (\alpha |g\rangle_A + \beta |e\rangle_A) |g\rangle_B |0_1 0_2\rangle + \gamma |g\rangle_A |g\rangle_B |1_1 0_2\rangle \\ &\xrightarrow{\pi_{e0g1}} |g\rangle_A |g\rangle_B (\alpha |0_1 0_2\rangle + \gamma |1_1 0_2\rangle + \beta |0_1 1_2\rangle). \end{aligned} \quad (\text{S7})$$

The receiver applies the time-reversed capture operations to the same temporal modes,

$$|g\rangle_A |g\rangle_B (\alpha |0_1 0_2\rangle + \gamma |1_1 0_2\rangle + \beta |0_1 1_2\rangle) \rightarrow |g\rangle_A (\alpha |g\rangle + \beta |e\rangle + \gamma |f\rangle)_B. \quad (\text{S8})$$

The qutrit is therefore carried by a hybrid encoding: $|g\rangle$ is the two-bin vacuum, $|f\rangle$ is a single photon in the first bin, and $|e\rangle$ is a single photon in the second bin.

For REG, the sender pulses are partial transfers. With the convention that a pulse angle θ produces amplitudes $\cos(\theta/2)$ and $\sin(\theta/2)$, the ideal sequence starts from $|e\rangle_A |g\rangle_B |0_1 0_2\rangle$. The first partial $e0g1$ pulse has $\theta_e = 2 \arctan(1/\sqrt{2})$, so that

$$|e\rangle_A |g\rangle_B |0_1 0_2\rangle \rightarrow \sqrt{\frac{2}{3}} |e\rangle_A |g\rangle_B |0_1 0_2\rangle + \frac{1}{\sqrt{3}} |g\rangle_A |g\rangle_B |1_1 0_2\rangle. \quad (\text{S9})$$

Local π_{ef} and π_{ge} rotations on node A relabel the stored branches,

$$\sqrt{\frac{2}{3}} |f\rangle_A |g\rangle_B |0_1 0_2\rangle + \frac{1}{\sqrt{3}} |e\rangle_A |g\rangle_B |1_1 0_2\rangle. \quad (\text{S10})$$

A subsequent $f0g1$ partial pulse with $\theta_f = \pi/2$ gives

$$\frac{1}{\sqrt{3}} |f\rangle_A |g\rangle_B |0_1 0_2\rangle + \frac{1}{\sqrt{3}} |g\rangle_A |g\rangle_B |0_1 1_2\rangle + \frac{1}{\sqrt{3}} |e\rangle_A |g\rangle_B |1_1 0_2\rangle. \quad (\text{S11})$$

Full capture of the first bin by $e0g1$ and of the second bin by $f0g1$ maps the three branches to

$$|\Psi_{\text{qutrit}}\rangle = \frac{1}{\sqrt{3}} (|fg\rangle + |gf\rangle + |ee\rangle), \quad (\text{S12})$$

up to local phases. This protocol contains no $|1_11_2\rangle$ flying-photon component. The entanglement is generated through three coherent alternatives: no photon, a first-bin photon, or a second-bin photon. Therefore at most one photon is exposed to propagation loss in the link.

C. Tomography measurement bases and readout correction

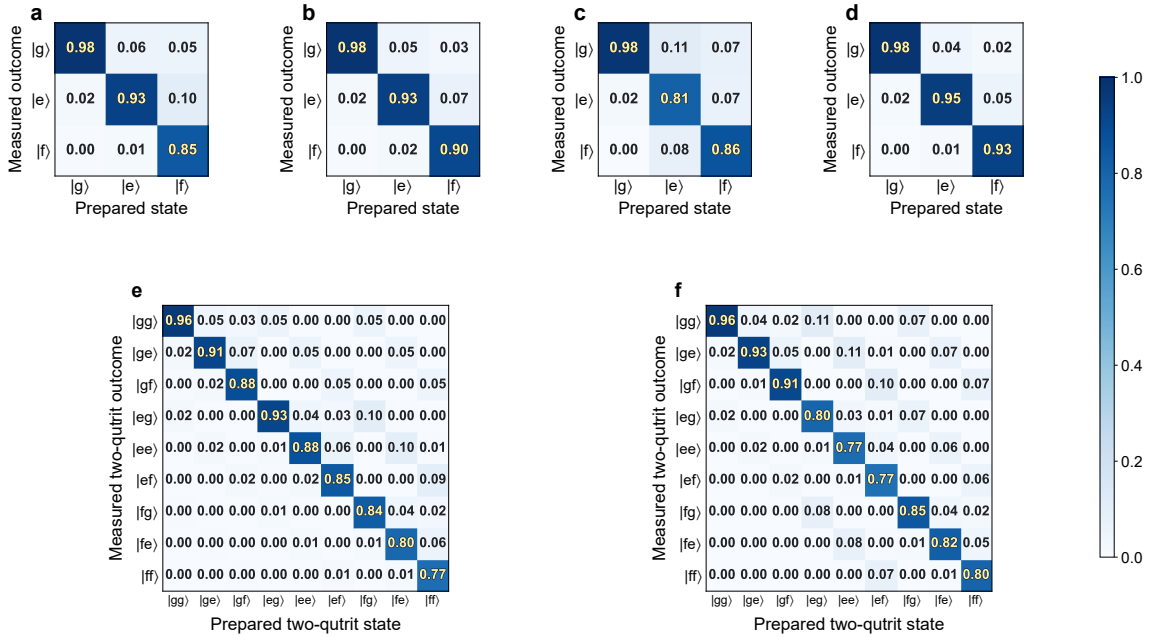


FIG. S8: **Qutrit readout correction.** (a,b) Single-qutrit readout assignment matrices measured before the qutrit state-transfer QST/QPT experiment and used for that reconstruction. (c,d) Single-qutrit readout assignment matrices measured before the REG tomography experiment and used for that reconstruction. (e,f) Full two-qutrit correction matrices $M_A \otimes M_B$ used for the corresponding tomography datasets. Numerical values are written in each matrix element to make the correction transparent.

Figure S8 gives the assignment matrices used for heterodyne qutrit readout and state discrimination [9, 10]. These matrices are independent calibration data, not adjustable

post-processing parameters. Panels a and b were measured before the qutrit state-transfer QST/QPT datasets, and panels c and d were measured before the REG tomography dataset, using the same readout pulses, integration window and state-discrimination procedure as the corresponding tomography run. Once measured, the assignment matrices are kept fixed for every input state, every analysis basis and every repetition in that run. No entry of the matrices is fitted to the reconstructed density matrix, to the ideal target state or to the beyond-qubit benchmarks.

Three-level readout errors are the dominant SPAM imperfection in the tomography data, so the assignment matrices are measured in the same experimental configuration as the tomography experiments and then applied as a fixed linear response correction. Before readout, tomography pulses rotate the desired qutrit coherence into a population difference. For one qutrit we use the nine analysis settings

$$\begin{aligned} \mathcal{A}_{1q} = \{ & I, R_x^{ge}(\pi/2), R_y^{ge}(\pi/2), R_x^{ef}(\pi/2), R_y^{ef}(\pi/2), \\ & R_x^{ef}(\pi/2)R_x^{ge}(\pi/2), R_y^{ef}(\pi/2)R_x^{ge}(\pi/2), R_x^{ef}(\pi/2)R_y^{ge}(\pi/2), R_y^{ef}(\pi/2)R_y^{ge}(\pi/2)\}. \end{aligned} \quad (\text{S13})$$

Here $R_{x,y}^{mn}(\pi/2)$ denotes a calibrated $\pi/2$ rotation in the $\{|m\rangle, |n\rangle\}$ subspace. This over-complete analysis set accesses the populations and the real and imaginary parts of ρ_{ge} , ρ_{gf} and ρ_{ef} . The non-adjacent $|g\rangle$ - $|f\rangle$ coherence is not measured with a direct gf pulse; it is mapped to a population difference through composite rotations on the adjacent ge and ef transitions. After readout correction, the density matrix is obtained by maximum-likelihood estimation constrained to be Hermitian, positive semidefinite and unit trace.

For two-qutrit state tomography, the single-qutrit analysis settings are applied independently to both nodes. This gives $9^2 = 81$ joint analysis settings. For each setting, the two qutrits are read out in the product basis $\{|gg\rangle, |ge\rangle, |gf\rangle, |eg\rangle, \dots, |ff\rangle\}$, producing a nine-component probability vector. These probability vectors reconstruct the full 9×9 density matrix used for the REG fidelity, negativity [11–13], dense-coding capacity [14–16] and CGLMP calculations [17].

The measured qutrit population vector \mathbf{p}_{meas} is related to the corrected population vector \mathbf{p} by

$$\mathbf{p}_{\text{meas}} = M\mathbf{p}, \quad (\text{S14})$$

where M_{ij} is the probability to assign the measurement outcome i when the prepared state

is j . The corrected probabilities are obtained as

$$\mathbf{p} = M^{-1} \mathbf{p}_{\text{meas}}. \quad (\text{S15})$$

For two-qutrit tomography, the assignment matrix is

$$M_{AB} = M_A \otimes M_B. \quad (\text{S16})$$

The same correction procedure is used for qutrit state-transfer QPT and for two-qutrit REG tomography. In qutrit process tomography, nine linearly independent qutrit input states are prepared on node A using calibrated local rotations in the $|g\rangle$ - $|e\rangle$ and $|e\rangle$ - $|f\rangle$ subspaces. In the data shown in the main text, these states are generated from $|g\rangle$ by the gate pairs

$$\begin{aligned} & (I, I), (X_{ge}, I), (X_{ge}, X_{ef}), (X_{ge}/2, I), (X_{ge}/2, X_{ef}), \\ & (X_{ge}, X_{ef}/2), (Y_{ge}/2, I), (Y_{ge}/2, X_{ef}), (X_{ge}, Y_{ef}/2), \end{aligned} \quad (\text{S17})$$

where the first and second entries denote the ge - and ef -subspace preparation rotations, respectively. For each input state, we reconstruct the prepared state before transfer and the received state after transfer using the same readout-corrected maximum-likelihood tomography procedure. The resulting input-output density-matrix pairs are used to reconstruct the qutrit process matrix in the Gell-Mann basis. These maximum-likelihood density matrices are used for fidelity and information-metric evaluation.

We also run the tomography pipeline without inverting the assignment matrices as a diagnostic of the detector response. This uncorrected reconstruction is the detector-convolved density matrix, not the state at the output of the quantum operation. For single-qutrit transfer, the mean final-state fidelity changes from 83.68% after correction to 78.26% without correction, while the process fidelity is nearly unchanged in the present reconstruction. For the two-qutrit REG data, the effect is larger because the nine-outcome readout matrix is a tensor product of two imperfect three-state measurements. As expected, leaving the detector response uncorrected reduces the state fidelity, negativity, tomography-inferred dense-coding capacity and tomography-inferred CGLMP value computed from the two-qutrit density matrix.

We do not use the uncorrected values as separate performance benchmarks. They quantify the detector bias that the independently measured assignment matrices remove. All main-text tomography values use the same fixed assignment matrices measured in the corresponding experimental configuration. The correction is a linear inversion of the readout

response; it does not use postselection or a fit to the target state. The central robustness test is therefore not whether the detector-convolved matrices by themselves exceed the high-dimensional bounds, but whether the readout-corrected conclusions survive realistic uncertainty in the independently calibrated assignment matrices. This test is carried out in Sec. III by resampling the assignment matrices and recomputing all beyond-qubit benchmarks.

D. Primitive transfer and REG QST diagnostics

Figure S9 gives tomography diagnostics for the elementary $e0g1$ and $f0g1$ operations. Panels a and b are effective two-level state-transfer reconstructions. The $e0g1$ primitive transfers the $\{|g\rangle, |e\rangle\}$ subspace. The $f0g1$ primitive transfers the $\{|g\rangle, |f\rangle\}$ excitation and then maps the receiver population back to the $\{|g\rangle, |e\rangle\}$ readout subspace with a local π_{ef} pulse.

Panels c and d are two-qutrit QST results for REG sequences constructed from the same primitives. They are density-matrix reconstructions of partially transferred states, not additional process matrices. The simulations use the same cascaded master-equation model and calibrated channel parameters as the main-text state-transfer and REG simulations.

These primitive fidelities are diagnostic benchmarks for the building blocks. The high-dimensional channel benchmark is the full qutrit QPT data in the main text and in Fig. S10. The primitive diagnostics are included here to show that the same calibrated transfer operations used in the main sequence behave consistently at the level of individual transitions.

E. Phase and matrix-distance diagnostics

The real parts of the qutrit process matrix and the REG density matrix carry the main physical signal and are shown in the main text as compact overlaid matrix panels. Figure S10 and Table S2 provide the complementary diagnostics needed to read those panels quantitatively. The imaginary components in Fig. S10a,b are sensitive to residual phase errors after calibration of the transfer frame and local virtual- Z corrections. The residual maps in Fig. S10c,d show the element-wise real-part differences between the experimental matrices and the corresponding pulse-level simulations, while Table S2 reports the associated matrix

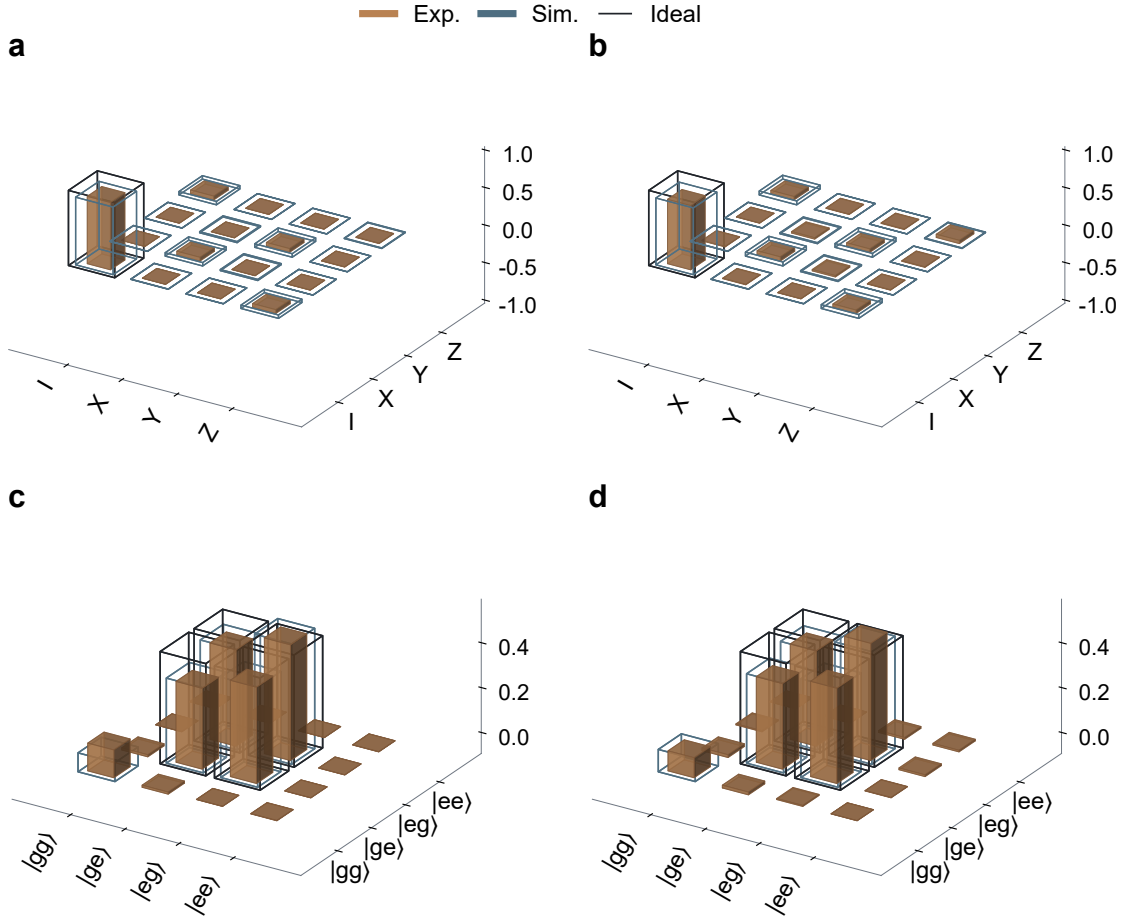


FIG. S9: **Primitive transfer and REG QST diagnostics.** (a,b) Effective two-level state-transfer tomography for the $e0g1$ and $f0g1$ primitives. Filled bars denote experiment, blue outlines denote pulse-level simulation, and black outlines denote the ideal transfer operation in the corresponding two-level subspace. (c,d) Two-qutrit QST of REG states generated with the $e0g1$ and $f0g1$ primitives, respectively. These panels show reconstructed REG density matrices, not process matrices.

distances.

The qutrit process matrix is reconstructed in the Gell-Mann operator basis from the measured input-output state pairs. The experimental process fidelity is $77.12\% \pm 0.10\%$, and the average final-state fidelity over the nine tested qutrit states is 83.68% . The simulated values are 84.10% and 89.45% , respectively. Both experiment and simulation exceed the qubit-channel bound for average qutrit state transfer, i.e. the maximum Haar-averaged

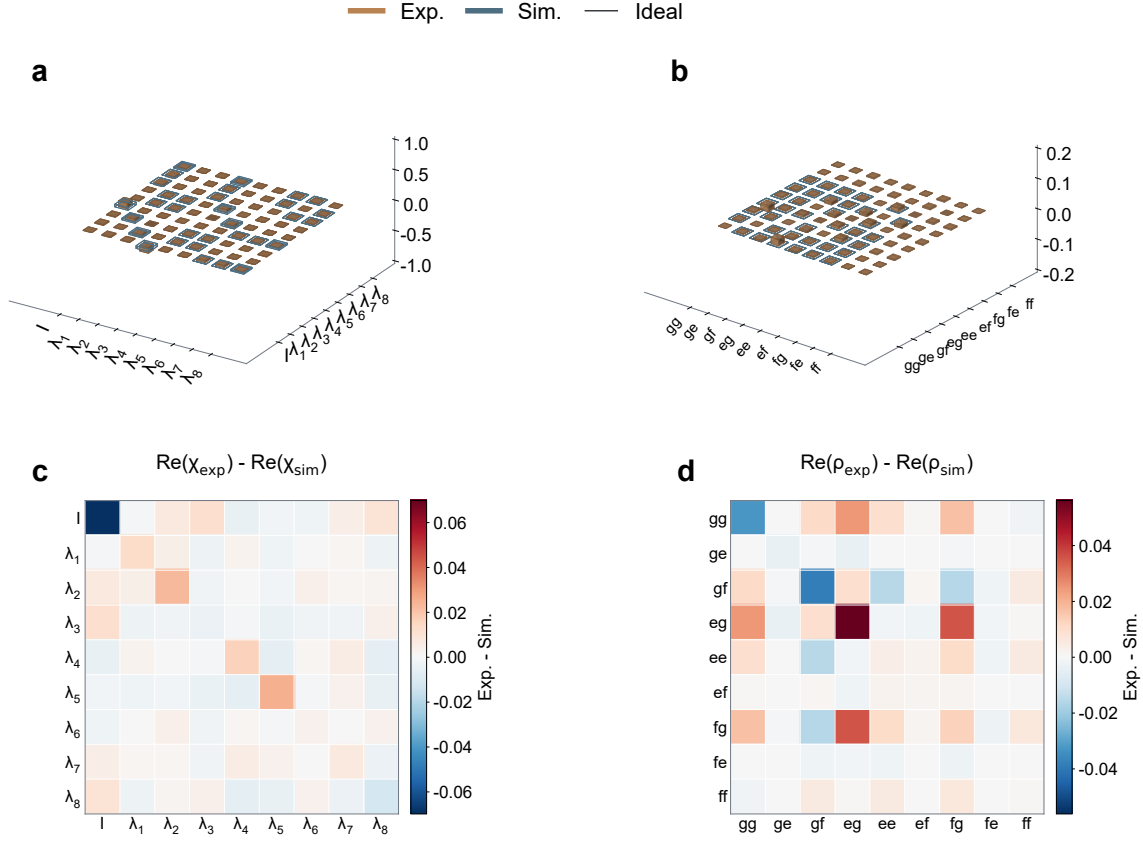


FIG. S10: **Phase and residual matrix diagnostics for qutrit transfer and REG.**

(a) Imaginary part of the qutrit state-transfer process matrix in the Gell-Mann operator basis. (b) Imaginary part of the phase-aligned two-qutrit REG density matrix. (c) Residual real part of the qutrit-transfer process matrix, $\text{Re}(\chi_{\text{exp}}) - \text{Re}(\chi_{\text{sim}})$. (d) Residual real part of the REG density matrix, $\text{Re}(\rho_{\text{exp}}) - \text{Re}(\rho_{\text{sim}})$. Experimental filled bars, simulated blue outlines and ideal black outlines are overlaid in **a,b**; **c,d** use centered color scales for experiment–simulation residuals.

fidelity $3/4$ obtainable when an arbitrary qutrit is transmitted through an effectively two-dimensional quantum channel.

To quantify the visual agreement between reconstructed and simulated matrices, we use the matrix distance

$$D(\rho_{\text{exp}}, \rho_{\text{sim}}) = \sqrt{\text{Tr} [(\rho_{\text{exp}} - \rho_{\text{sim}})^2]}. \quad (\text{S18})$$

This follows the matrix-distance convention used for microwave-link process comparisons in

Ref. [7]. It is zero for identical matrices and increases as the reconstructed matrix moves away from the simulation. For the qutrit-transfer process matrix in main-text Fig. 3, the mean reconstructed matrix and the simulated matrix give $D = 0.141$.

For REG, the target state is

$$|\psi_{\text{REG}}\rangle = \frac{1}{\sqrt{3}} (|gf\rangle + |ee\rangle + |fg\rangle), \quad (\text{S19})$$

up to local phases. The raw density matrix includes deterministic phases accumulated during the pulse sequence. Before evaluating the phase-aligned fidelity and dense-coding capacity, we remove these phases by local virtual-Z rotations. The extracted ef -frame corrections are 0.911 rad on node A and -2.035 rad on node B.

After phase alignment, the REG fidelity is $81.21\% \pm 0.37\%$. The reconstructed matrix retains the three target populations and the three pairwise coherences in the $\{|gf\rangle, |ee\rangle, |fg\rangle\}$ manifold. The corresponding simulation gives a REG fidelity of 83.36% , using the same loss and dephasing parameters as the qutrit-transfer simulation.

The imaginary components in Fig. S10a,b remain small compared with the dominant real coherences. The residual maps in Fig. S10c,d further show that the remaining experiment–simulation differences are distributed over small off-diagonal and leakage-related components rather than a single large coherent phase error. This supports the interpretation that the reconstructed qutrit transfer and REG state are mainly limited by finite transfer efficiency, internal loss and dephasing.

TABLE S2: Matrix-distance comparison between experiment and pulse-level simulation. The mean-matrix distance is calculated between the readout-corrected mean experimental matrix and the simulated mean matrix. The repetition-level value is the mean and standard deviation of the distance between each experimental tomography repetition and the same simulated mean matrix.

Figure	Matrix	D	Repetition-level D
Main-text Fig. 2	$e0g1$ primitive process matrix	0.029	0.039 ± 0.014
Main-text Fig. 2	$f0g1$ primitive process matrix	0.068	0.085 ± 0.016
Main-text Fig. 3	qutrit-transfer process matrix	0.141	0.142 ± 0.002
Main-text Fig. 4	REG density matrix	0.119	0.120 ± 0.003

III. BEYOND-QUBIT BENCHMARKS AND ROBUSTNESS CHECKS

A. Metric definitions and readout-correction confidence

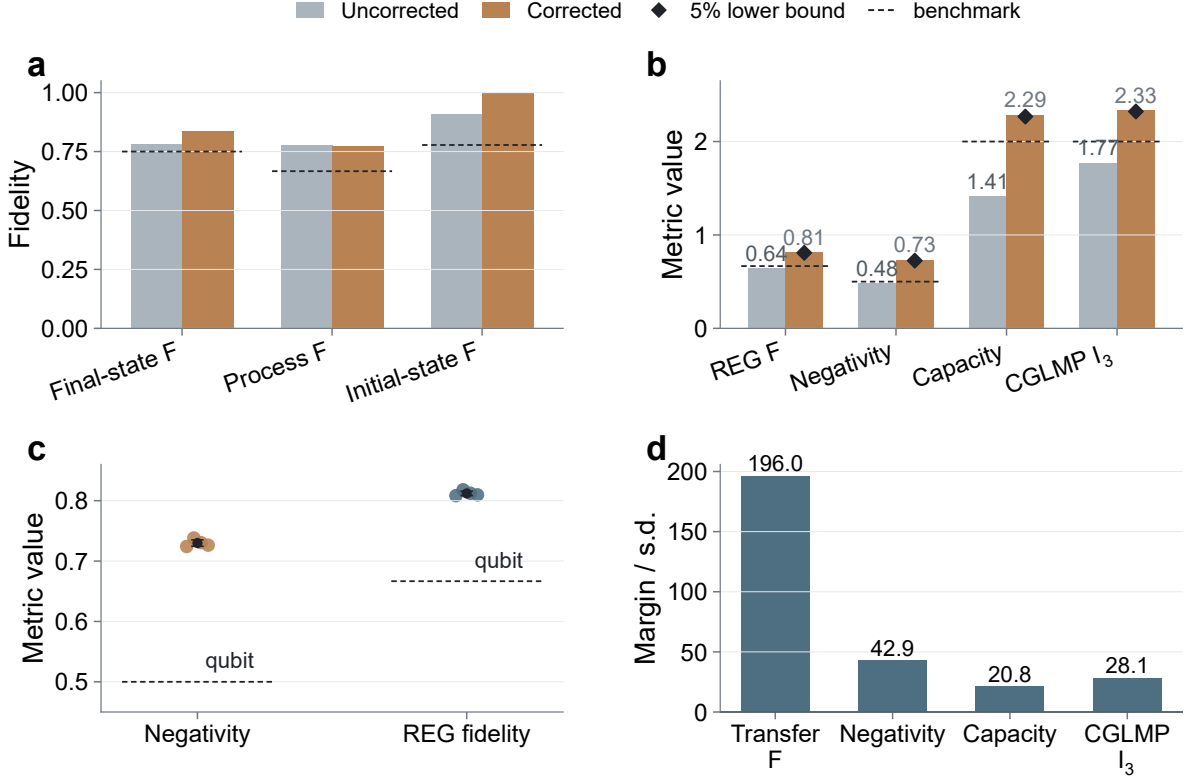


FIG. S11: **Readout-correction sensitivity and repetition-level confidence.** (a) Transfer-state and process fidelities reconstructed with and without the independently calibrated readout-assignment correction. Short dashed segments mark the relevant bounds for the three different quantities. (b) REG metrics reconstructed with and without the same correction. Black diamonds mark the 5th-percentile lower bounds obtained by Monte-Carlo resampling of the calibrated readout-assignment matrices. (c) Repetition-level spread of the readout-corrected REG negativity and phase-aligned REG fidelity. Dots are individual tomography repetitions, black markers show the mean and one standard deviation, and dashed segments mark the two-qubit bounds. (d) Statistical margin above the relevant qubit or local benchmark, normalized by the repetition-level standard deviation.

Figure S11 is the main robustness check for the beyond-qubit claims. The quantities plotted there are the Schmidt-number witness [18], negativity [11–13], tomography-inferred

dense-coding capacity [14–16], and tomography-inferred CGLMP parameter [17]. The logic is deliberately conservative. We first compare corrected and detector-convolved reconstructions to show the size of the readout bias. We then resample the independently calibrated assignment matrices and repeat the full reconstruction. The main-text claims use the readout-corrected tomography with the measured assignment matrices in Fig. S8; the black diamonds in Fig. S11 show that the relevant conclusions remain above their limits under this assignment-matrix uncertainty.

In Fig. S11(a), we compare the reconstructed final-state fidelity, the qutrit process fidelity, and the input-state fidelity before and after applying the calibrated readout-assignment correction. The final-state fidelity is the mean fidelity of the transferred qutrit states at the receiver, and its dashed segment marks the average-fidelity benchmark $3/4$ for transferring an arbitrary qutrit through an effectively two-dimensional quantum channel. The qutrit process fidelity has a different normalization. Using $F_{\text{avg}} = (dF_{\text{pro}} + 1)/(d + 1)$ with $d = 3$, the same $F_{\text{avg}} = 3/4$ benchmark corresponds to $F_{\text{pro}} = 2/3$, shown as the dashed segment for the process-fidelity group. The input-state fidelity is a state-preparation diagnostic for the nine QPT input states rather than a channel metric. For this finite input set, the best average fidelity obtainable with a fixed two-dimensional qutrit subspace is $7/9$, obtained from the two largest eigenvalues of the average ideal input-state density matrix. This finite-set bound is shown for the input-state fidelity group.

In Fig. S11(b), we make a comparison between four REG-derived quantities before and after readout correction in their native units: the phase-aligned target-state overlap, the negativity, the tomography-inferred dense-coding capacity and the tomography-inferred CGLMP value I_3 . The dashed segments mark the corresponding bounds: $2/3$ for the REG fidelity, 0.5 for the two-qubit negativity bound, 2 bits for the two-qubit dense-coding limit, and $I_3 = 2$ for locality. To test sensitivity to the calibrated assignment matrices, we resample the two qutrit readout matrices with a conservative Dirichlet model using 4000 effective calibration shots per prepared level and a 0.3% symmetric drift floor. This drift floor accounts for slow readout-response variations not captured by finite-shot Dirichlet sampling; it is applied symmetrically over the three possible outcomes and is not fitted to the reconstructed density matrix or to any benchmark value. Its magnitude is chosen as a conservative sub-percent broadening of the independently calibrated assignment matrices. The black diamonds are the 5th-percentile lower bounds from 400 resampled reconstructions. Even the worst sampled

reconstruction gives $F_{\Psi_3} = 0.8036$, $\mathcal{N} = 0.7176$, $C = 2.242$ bits and $I_3 = 2.307$, all above the corresponding bounds. Thus the beyond-qubit conclusions are not set by a favorable choice of a single readout matrix.

Fig. S11(c) shows the repetition-level spread of the two central REG quantities after readout correction: negativity and phase-aligned REG fidelity. The excess above the two-qubit bounds is therefore not set by a single outlying reconstruction.

Fig. S11(d) plots the margin $(\bar{x} - x_{\text{bound}})/\sigma_x$ for four benchmark quantities. This is a compact confidence diagnostic based on repetition-level spread. Systematic effects from readout calibration, pulse calibration and tomography reconstruction are treated separately through the readout-correction comparison and the simulation model.

For the REG-state fidelity, the relevant two-level entanglement bound is $2/3$ because for a target maximally entangled qutrit state with three equal Schmidt coefficients, the maximum overlap with any Schmidt-rank-two state is $2/3$. The measured phase-aligned fidelity $F_{\Psi_3} = 0.8121 \pm 0.0037$ therefore witnesses Schmidt number 3. Under the readout-assignment resampling described above, the 5th-percentile lower bound is $F_{\Psi_3} = 0.8086$, and the worst sampled value is $F_{\Psi_3} = 0.8036$, still well above $2/3$. This is the qubit-entanglement bound used in Fig. S11(c).

The negativity is computed from the partial transpose [11, 12],

$$\mathcal{N}(\rho) = \frac{\|\rho^{T_B}\|_1 - 1}{2}. \quad (\text{S20})$$

For a maximally entangled two-qubit state, the maximum negativity is 0.5. The measured ensemble-averaged REG state has $\mathcal{N} = 0.7297 \pm 0.0054$, exceeding the two-qubit bound and confirming that the generated entanglement cannot be represented as a maximally entangled two-level pair. The log-negativity is 1.2984 ± 0.0063 . The readout-assignment resampling gives a 5th-percentile lower bound $\mathcal{N} = 0.7248$ and a worst sampled value $\mathcal{N} = 0.7176$, again above the two-qubit maximum.

Following the standard dense-coding capacity expression for a shared bipartite state [14, 16], the dense-coding capacity is evaluated from the reconstructed shared state as

$$C = \log_2 d + S(\rho_B) - S(\rho_{AB}), \quad (\text{S21})$$

with local dimension $d = 3$. The measured phase-aligned ensemble-averaged density matrix gives $C = 2.273 \pm 0.014$ bits. This value exceeds both the classical qutrit communication limit

$\log_2 3$ and the two-qubit dense-coding limit of 2 bits, demonstrating the channel-capacity advantage provided by the high-dimensional entangled resource. The corresponding 5th-percentile lower bound under readout-assignment resampling is $C = 2.267$ bits, and the worst sampled value is $C = 2.242$ bits.

Finally, we evaluate the Collins-Gisin-Linden-Massar-Popescu (CGLMP) parameter I_3 from the reconstructed two-qutrit density matrix [17]. The CGLMP inequality is the standard Bell inequality for two parties, two measurement settings per party, and three outcomes per measurement. We first express the physical target state $(|gf\rangle + |ee\rangle + |fg\rangle)/\sqrt{3}$ in the logical basis $(|00\rangle + |11\rangle + |22\rangle)/\sqrt{3}$ by reversing the level order of node B. In this logical basis, Alice chooses one of two measurements A_0, A_1 , Bob chooses one of two measurements B_0, B_1 , and all outcomes are evaluated modulo 3. We use

$$I_3 = P(A_0 - B_0 = 0) + P(B_0 - A_1 = 1) + P(A_1 - B_1 = 0) + P(B_1 - A_0 = 0) \\ - P(A_0 - B_0 = -1) - P(B_0 - A_1 = 0) - P(A_1 - B_1 = -1) - P(B_1 - A_0 = -1), \quad (\text{S22})$$

where $P(A_x - B_y = k) = \sum_{a=0}^2 P(a, b = a - k \bmod 3 | x, y)$. Any local hidden-variable model satisfies $I_3 \leq 2$.

The projective measurement bases are the usual CGLMP bases optimized for the maximally entangled qutrit state,

$$|a_x\rangle = \frac{1}{\sqrt{3}} \sum_{j=0}^2 \omega^{j(a+\alpha_x)} |j\rangle, \quad |b_y\rangle = \frac{1}{\sqrt{3}} \sum_{j=0}^2 \omega^{j(-b+\beta_y)} |j\rangle, \quad (\text{S23})$$

with $\omega = \exp(2\pi i/3)$, $(\alpha_0, \alpha_1) = (0, 1/2)$, and $(\beta_0, \beta_1) = (1/4, -1/4)$. For a density matrix ρ , the probabilities are computed as

$$P(a, b | x, y) = \langle a_x, b_y | \rho | a_x, b_y \rangle. \quad (\text{S24})$$

With this convention, the ideal maximally entangled qutrit target gives $I_3 = 2.873$, while the local realistic bound remains 2. The reconstructed state gives $I_3 = 2.332 \pm 0.012$, above the local bound and consistent with nonlocal correlations available from the generated two-qutrit entangled state. The 5th-percentile lower bound under readout-assignment resampling is $I_3 = 2.322$, and the worst sampled value is $I_3 = 2.307$. Since this quantity is inferred from the reconstructed density matrix rather than obtained from a direct loophole-free Bell experiment with independently chosen measurement settings, we describe it as a tomography-inferred CGLMP violation.

Together, these metrics show the same high-dimensional advantage from three complementary viewpoints: the entanglement negativity exceeds the two-qubit maximum, the tomography-inferred dense-coding capacity exceeds the qubit limit, and the tomography-inferred correlations exceed the qutrit CGLMP local bound. The readout-resampling test in Fig. S11 is the key systematic check supporting these statements, because it propagates uncertainty in the independently measured qutrit assignment matrices through the same reconstruction pipeline used for the main-text numbers.

IV. PULSE-LEVEL SIMULATION, DEPHASING MODEL AND ERROR BUDGET

A. Cascaded master-equation model and dephasing implementation

The simulations use the same pulse-level cascaded model used to reproduce the primitive-calibration data. Each node is represented by a truncated transmission resonator a_j and a truncated transmon mode b_j , with $j = A, B$. The tensor order is (a_A, q_A, a_B, q_B) , and the transmon Hilbert space is restricted to the qutrit manifold $\{|g\rangle, |e\rangle, |f\rangle\}$. Protocol-level parameters are set by the intended operation: full-transfer pulses implement the two qutrit-transfer primitives, whereas reduced pulse areas implement the partial transfers used for remote entanglement generation. The chirp calibrations described in Sec. IG are treated as part of the calibrated drive frame. We therefore set the residual deterministic detunings of the $e0g1$ and $f0g1$ pulses to zero and do not add separate ac-Stark-shift correction terms in the rotating-frame Hamiltonian. For one quasi-static detuning realization, the Hamiltonian is

$$H(t)/\hbar = H_{\text{stat}}/\hbar + H_{\text{casc}}/\hbar + H_{e0g1}(t)/\hbar + H_{f0g1}(t)/\hbar + H_{\text{loc}}(t)/\hbar + H_{\text{noise}}(\delta)/\hbar. \quad (\text{S25})$$

The static part keeps the weak auxiliary-resonator Kerr terms and the dispersive shifts that are present in the pulse-level notebooks,

$$H_{\text{stat}}/\hbar = \sum_{j=A,B} \left[\frac{K_j}{2} a_j^{\dagger 2} a_j^2 + \chi_j a_j^{\dagger} a_j b_j^{\dagger} b_j \right], \quad (\text{S26})$$

with the residual resonator detuning set to zero at the matched operating point. The directional waveguide connection is written in the Gardiner–Carmichael cascaded form

$$H_{\text{casc}}/\hbar = -\frac{i}{2} \sqrt{\eta_c \kappa_{T,A} \kappa_{T,B}} \left(a_A a_B^{\dagger} - a_A^{\dagger} a_B \right), \quad (\text{S27})$$

where $\kappa_{T,A}/2\pi = \kappa_{T,B}/2\pi \simeq 10$ MHz is the loaded auxiliary-resonator linewidth at the high-bandwidth Purcell-filter setting and $\eta_c = 0.92$ is the channel efficiency used in the main-text simulations.

The two transfer primitives are implemented as different effective interactions, not as the same direct qutrit-lowering operator. For the $e0g1$ primitive, flux modulation activates the resonant exchange

$$H_{e0g1}(t)/\hbar = \sum_{j=A,B} g_{e,j}(t) \left(|0, e\rangle_j \langle 1, g| + |1, g\rangle_j \langle 0, e| \right), \quad (\text{S28})$$

which transfers $|e, 0\rangle \leftrightarrow |g, 1\rangle$ between the qutrit and the auxiliary resonator. For the $f0g1$ primitive, the cavity-assisted Raman process is modeled by the three-wave-mixing effective term used in the original simulation,

$$H_{f0g1}(t)/\hbar = \sum_{j=A,B} \frac{g_{f,j}(t)}{\sqrt{2}} \left(b_j^{\dagger 2} a_j + a_j^{\dagger} b_j^2 \right), \quad (\text{S29})$$

which couples $|f, 0\rangle \leftrightarrow |g, 1\rangle$ in the qutrit subspace. In the experiments analyzed here, $g_{e,j}(t)$ and $g_{f,j}(t)$ are chirp-corrected 200 ns sine envelopes. Table S3 lists the effective peak couplings used in the pulse-level simulations.

TABLE S3: **Effective coupling parameters used in the pulse-level simulations for**

Figs. 2–4. All rows use chirp-corrected 200 ns sine envelopes for the addressed photon-mediated primitive. The listed values are the peak resonant-frame couplings $g_j^{\max}/2\pi$ used in the cascaded master-equation simulations, not arbitrary waveform-generator voltages. The Fig. 3 qutrit-transfer sequence applies $f0g1$ followed by $e0g1$, whereas the Fig. 4 REG sequence applies $e0g1$ followed by $f0g1$.

Use	Primitive	Target operation	$g_A^{\max}/2\pi$	$g_B^{\max}/2\pi$
Fig. 2 dynamics	$e0g1$	full transfer	3.90 MHz	3.90 MHz
Fig. 2 dynamics	$f0g1$	full transfer	3.85 MHz	3.35 MHz
Fig. 3 QPT	$f0g1$	π transfer	4.00 MHz	3.45 MHz
Fig. 3 QPT	$e0g1$	π transfer	3.90 MHz	3.90 MHz
Fig. 4 REG	$e0g1$	partial, $P = 1/3$	1.31 MHz	3.92 MHz
Fig. 4 REG	$f0g1$	partial, $P = 1/2$	1.78 MHz	4.25 MHz

The local-control Hamiltonian contains only the qutrit rotations used in the protocols,

$$H_{\text{loc}}(t)/\hbar = \sum_{j=A,B} \left[\frac{\Omega_{ge,j}(t)}{2} (|g_j\rangle \langle e_j| + \text{h.c.}) + \frac{\Omega_{ef,j}(t)}{2} (|e_j\rangle \langle f_j| + \text{h.c.}) \right], \quad (\text{S30})$$

with Gaussian π_{ge} , $\pi/2_{ge}$, π_{ef} , and $\pi/2_{ef}$ pulses inserted according to the state-transfer or REG pulse sequence.

The simulations are integrated with QuTiP [19, 20]. In the implementation, Eq. (S27) is combined with the collective radiative collapse operator

$$C_{\text{casc}} = \sqrt{\eta_c \kappa_{T,A}} a_A + \sqrt{\kappa_{T,B}} a_B, \quad (\text{S31})$$

and the channel-loss operator

$$C_{\text{loss,A}} = \sqrt{(1 - \eta_c) \kappa_{T,A}} a_A. \quad (\text{S32})$$

This representation is equivalent to the usual unidirectional cascaded master equation and enforces propagation from node A to node B. For a fixed detuning realization,

$$\frac{d\rho}{dt} = -i[H(t), \rho] + \mathcal{D}[C_{\text{casc}}]\rho + \mathcal{D}[C_{\text{loss,A}}]\rho + \sum_m \mathcal{D}[C_m]\rho, \quad (\text{S33})$$

where

$$\mathcal{D}[C]\rho = C\rho C^\dagger - \frac{1}{2}\{C^\dagger C, \rho\}. \quad (\text{S34})$$

The remaining C_m describe internal auxiliary-resonator loss and qutrit relaxation,

$$\begin{aligned} C_{\text{int},j} &= \sqrt{\kappa_{\text{int},j}} a_j, \\ C_{ge,j} &= \sqrt{1/T_{1,ge,j}} |g_j\rangle \langle e_j|, \quad C_{ef,j} = \sqrt{1/T_{1,ef,j}} |e_j\rangle \langle f_j|. \end{aligned} \quad (\text{S35})$$

The intrinsic auxiliary-resonator losses used in the present simulations are $\kappa_{\text{int},A}/2\pi = 0.0208$ MHz and $\kappa_{\text{int},B}/2\pi = 0.0176$ MHz, corresponding to the angular-frequency rates $0.1308 \mu\text{s}^{-1}$ and $0.1104 \mu\text{s}^{-1}$. The independently measured $T_{1,ge}$ and $T_{1,ef}$ values are listed in Fig. S3. We do not quote a standard deviation for a single simulated fidelity; when an ensemble over detuning samples is used, the ensemble spread is a numerical-convergence diagnostic rather than an experimental uncertainty.

The main simulations do not use Markovian pure-dephasing collapse operators. Instead, the dominant dephasing is treated as quasi-static $1/f$ -like detuning noise. This choice is motivated by the Ramsey data: after the relaxation-limited decay is fixed by T_1 , the remaining

envelope is closer to a Gaussian decay than to a single exponential decay. A Markovian pure-dephasing model is useful as a comparison, but it continuously removes phase information during every part of the sequence and therefore over-penalizes the multi-pulse qutrit-transfer and REG protocols.

For one realization, we sample

$$\delta = (\delta_{ge,A}, \delta_{ef,A}, \delta_{ge,B}, \delta_{ef,B}), \quad \delta_\mu \sim \mathcal{N}(0, \sigma_\mu^2), \quad (\text{S36})$$

and add the static detuning Hamiltonian

$$H_{\text{noise}}(\delta)/\hbar = \sum_{j=A,B} [\delta_{ge,j} (|e_j\rangle \langle e_j| + |f_j\rangle \langle f_j|) + \delta_{ef,j} |f_j\rangle \langle f_j|]. \quad (\text{S37})$$

With this convention, the ge coherence accumulates $\delta_{ge,j}$, while the ef coherence accumulates $\delta_{ef,j}$. The final population traces, process matrices and density matrices are obtained by averaging the simulated output density matrix over the quasi-static ensemble, using the same tomography objects as in the experimental analysis.

The detuning widths are obtained from the T_1 -corrected Ramsey fits in Eq. (S1): $\sigma_{ge,A}/2\pi = 59.24$ kHz, $\sigma_{ge,B}/2\pi = 102.47$ kHz, $\sigma_{ef,A}/2\pi = 60.01$ kHz, and $\sigma_{ef,B}/2\pi = 102.18$ kHz. These experimentally extracted quasi-static detuning widths are used directly in the simulations of the primitive transfer dynamics, qutrit process tomography and two-qutrit state tomography, so that the same dephasing model is applied consistently to Figs. 2–4.

The model is nevertheless a fixed-parameter description of a long acquisition. The population-dynamics traces in Fig. 2 are acquired on a shorter time scale than the full qutrit QPT and two-qutrit QST datasets, whereas the tomography experiments average over many preparation, analysis and readout settings. During this longer acquisition, the two node frequencies, the $e0g1$ and $f0g1$ resonance conditions, the Purcell-filter operating point, the readout assignment matrices and the local phase reference can drift slowly. These drifts are not explicitly sampled in the pulse-level simulation, which uses one set of calibrated pulse amplitudes, resonant-frame couplings, readout-independent output states and virtual- Z phases. They can therefore contribute to the residual experiment–simulation differences in Figs. 3 and 4, especially in off-diagonal coherences and tomography-derived benchmarks, without changing the short-time transfer dynamics as strongly.

Figure S12 compares this quasi-static model with a Markovian pure-dephasing model using the same pulse-level settings as the main-text qutrit-transfer and REG simulations. The channel efficiency, internal resonator loss, pulse amplitudes and pulse timing are kept fixed. Only the dephasing implementation is changed. For the Markovian comparison, the Ramsey traces are refitted with an exponential envelope. After subtracting the relaxation-limited coherence decay, the resulting pure-dephasing times are $T_{\phi,ge,A}^M = 3.84 \mu\text{s}$, $T_{\phi,ge,B}^M = 1.71 \mu\text{s}$, $T_{\phi,ef,A}^M = 3.79 \mu\text{s}$, and $T_{\phi,ef,B}^M = 1.85 \mu\text{s}$. These times set the Lindblad dephasing rates used only for this comparison. In the quasi-static model, the dominant low-frequency detuning is constant during one experimental shot and changes between shots. This produces the measured Gaussian Ramsey envelope, but it does not erase coherence inside a 200 ns transfer pulse as strongly as the Markovian model. The difference between the two descriptions is modest for the qutrit state-transfer benchmarks: the Markovian simulation gives a process fidelity of 0.739 and a mean output-state fidelity of 0.839, compared with 0.841 and 0.895 from the quasi-static $1/f$ -like simulation. The difference is larger for REG, where the Markovian simulation gives a state fidelity of 0.728, negativity of 0.600, tomography-inferred dense-coding capacity of 1.791 bits and a tomography-inferred CGLMP value $I_3 = 2.052$, whereas the quasi-static simulation gives 0.834, 0.756, 2.242 bits and $I_3 = 2.417$ after first averaging the simulated density matrices. Thus, for qutrit state transfer the Markovian conversion changes the benchmarks only moderately, whereas for REG it suppresses the coherences that set the negativity, tomography-inferred dense-coding capacity and tomography-inferred CGLMP value much more strongly.

B. Sine and sech waveform comparison

The transfer experiments in the main text use 200 ns sine-shaped parametric pulses because they produce a near time-symmetric photon temporal mode for the calibrated bandwidth, are experimentally robust, have low spectral leakage, and can be applied reproducibly to both the $e0g1$ and $f0g1$ primitives. They are not the mathematical optimum for photon capture. In the ideal tunable-coupler problem, near-unit state-transfer efficiency is obtained by shaping the emission and capture rates so that the receiver implements the time reverse of the emitted photon mode [21, 22]. Related superconducting-circuit experiments have also used microwave control to generate and symmetrize shaped photons [23, 24]. Follow-

TABLE S4: **Markovian dephasing inputs and numerical comparison of dephasing**

models. The first table compares the pure-dephasing inputs extracted from the same Ramsey and T_1 data under two assumptions. T_ϕ^M is obtained from an exponential Ramsey envelope after subtracting the relaxation-limited coherence decay. $T_\phi^{1/f} \equiv \sqrt{2}/\sigma$ is obtained from the T_1 -corrected Gaussian Ramsey envelope used for the quasi-static $1/f$ -like detuning ensemble. Experimental benchmark values include one-standard-deviation statistical uncertainties. The two simulations use the same pulse-level parameters and differ only in the dephasing model.

Channel	T_2^M (μs)	T_ϕ^M (μs)	$\sigma/2\pi$ (kHz)	$T_\phi^{1/f}$ (μs)
ge, A	3.528	3.839	59.24	3.80
ge, B	1.647	1.711	102.47	2.20
ef, A	2.958	3.787	60.01	3.75
ef, B	1.631	1.854	102.18	2.20

Benchmark	Experiment	Quasi-static $1/f$	Markovian
QST process fidelity	0.771 ± 0.001	0.841	0.739
QST mean state fidelity	0.837 ± 0.0004	0.895	0.839
REG fidelity	0.812 ± 0.004	0.834	0.728
Negativity	0.730 ± 0.005	0.756	0.600
Dense-coding capacity (bits)	2.273 ± 0.014	2.242	1.791
CGLMP I_3	2.332 ± 0.012	2.417	2.052

TABLE S5: **Pulse-level comparison of sine and finite-window sech waveforms.**

The finite-window sech is constrained to the same 200 ns pulse window as the experimental sine pulse and is area matched to the sine pulse. Both rows use the same loss, T_1 , T_ϕ , η_c , κ_{int} , quasi-static detuning ensemble and REG averaged-density-matrix convention as the main-text simulations.

Waveform	Model	QST state F	QST process F	REG F	N	C (bits)	I_3
sine	with decoherence	0.8945	0.8410	0.8336	0.7556	2.2424	2.4172
finite-window sech	with decoherence	0.9056	0.8561	0.7809	0.6822	2.0871	2.2328

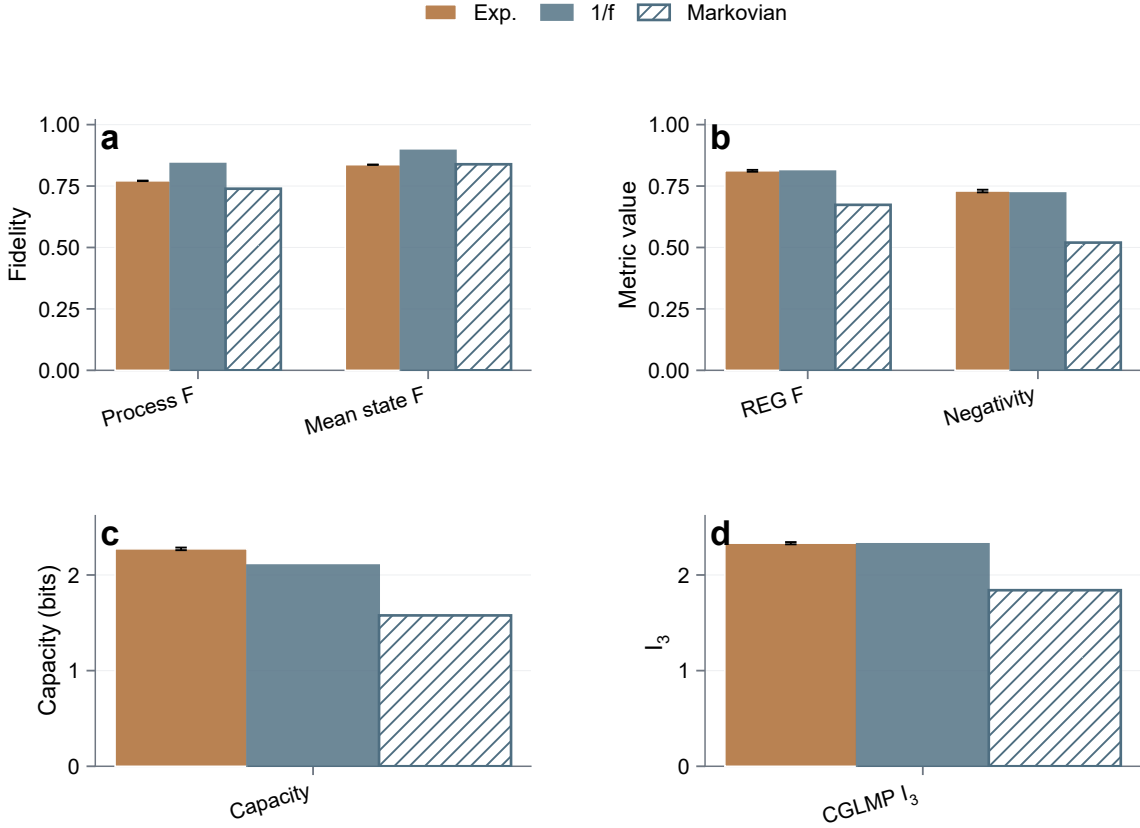


FIG. S12: **Comparison between Markovian and quasi-static dephasing models.**

(a) Qutrit state-transfer process fidelity and mean output-state fidelity. (b) REG state fidelity and negativity, plotted on a 0–1 scale. (c) Dense-coding capacity inferred from the REG density matrix. (d) Tomography-inferred CGLMP value I_3 from the same density matrix.

ing the pulse definition used in our original simulations, the sech envelope is written as $g(t) = g_0 / \cosh[(t - t_0)/\tau]$.

For this reason, the sine-pulse simulations should be interpreted as simulations of the actual experimental protocol rather than as an upper bound on the device. We include the sech comparison in Fig. S13 as a diagnostic of how much performance is left in pulse-shape optimization for a full emission-and-capture process. The first comparison keeps the same 200 ns pulse window as the experiment and matches the integrated coupling area. Since the matched transmission-resonator linewidth is $\kappa/2\pi \simeq 10$ MHz, we use a reference sech scale $\kappa_{\text{sech}}/2\pi = 5$ MHz, corresponding to $\tau = 1/\kappa_{\text{sech}} \simeq 31.8$ ns. Starting from the original

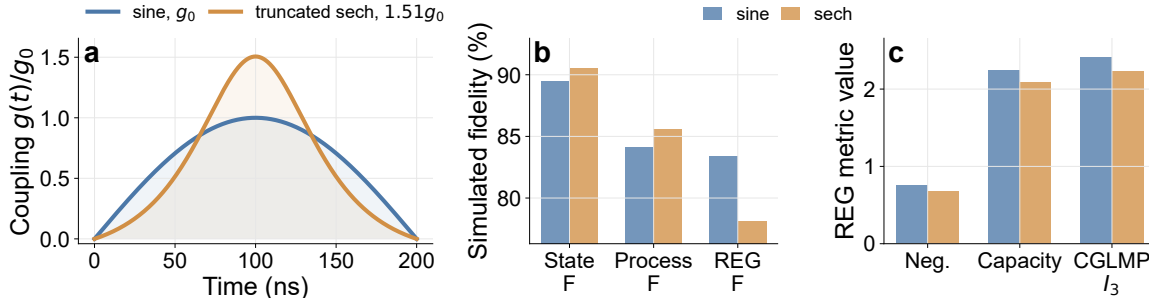


FIG. S13: **Waveform choice and linewidth-set sech-pulse comparison.** (a) The 200 ns sine control pulse used in the experiment and a finite-window sech pulse derived from $g(t) = g_0 / \cosh[(t - t_0)/\tau]$. The sech scale is set by $\kappa_{\text{sech}}/2\pi = 5$ MHz, motivated by the matched transmission-resonator linewidth $\kappa/2\pi \simeq 10$ MHz. The endpoint value of the sech window is subtracted before area matching so that the pulse returns to zero at the experimental pulse boundaries. Matching the pulse area requires a larger sech peak coupling, $g_{\text{sech}}^{\text{max}} \simeq 1.51g_0$. (b) Qutrit state-transfer fidelity, qutrit process fidelity and REG state fidelity using the experimental sine envelope and the linewidth-set finite-window sech envelope. (c) REG information metrics from the same decoherence model: negativity, tomography-inferred dense-coding capacity and tomography-inferred CGLMP value.

simulation definition $g(t) = g_0 / \cosh[(t - t_0)/\tau]$, we subtract the finite-window endpoint value and renormalize the peak before area matching, so that the plotted sech pulse starts and ends at zero rather than being visibly cut off. Under this constraint the peak coupling is $g_{\text{sech}}^{\text{max}} \simeq 1.51g_0$, larger than the sine-pulse peak.

The presence of the tunable Purcell-filter interface makes this optimization slightly different from the textbook single-resonator time-reversal problem. The emitted field is filtered by an additional mode before entering the transmission line, so the photon mode seen by the receiver is not exactly the mode generated by the auxiliary resonator alone. A receiver pulse designed for the unfiltered single-pole response is therefore not exactly optimal once the Purcell filter is included. For parameters close to the present device, this mode mismatch gives an order-1% capture-efficiency penalty. The numerical values are summarized in Table S5. With the current decoherence model, the finite-window sech pulse slightly improves the full qutrit-transfer state fidelity relative to the sine pulse.

The REG trend is different. Directly replacing the sine pulses by the finite-window

sech envelope lowers the reconstructed REG benchmarks in the present calculation, even though the same waveform improves the full-transfer channel. This should not be read as evidence that sech pulses are poor for entanglement generation. REG is a partial-transfer interference experiment rather than a complete state-transfer operation: the figure of merit depends on the relative amplitudes and phases of the $|gf\rangle$, $|ee\rangle$, and $|fg\rangle$ components, and the calibrated chirp must compensate the time-dependent frequency shift during the partial pulses. The REG waveform also has more free parameters than the direct substitution used here, including the two partial-transfer amplitudes, the relative timing of the two primitives, the chirped frequency trajectory and the local phase frame. A genuinely optimized REG sequence therefore has substantial remaining optimization space. The comparison here supports the practical choice of using the experimentally calibrated sine pulses throughout the main experiment, while showing that finite-window sech pulses can slightly improve the full qutrit-transfer channel.

C. Full-model inverse design of REG waveforms

The forward simulation discussed in the main text uses inverse-designed REG waveforms rather than a sine or sech waveform substituted into the experimental sequence. The design is based on the same cascaded input-output model used in the pulse-level simulations, and it retains the finite storage amplitudes of both transmission resonators instead of making a bad-cavity approximation. For either $e0g1$ or $f0g1$, we restrict the coherent dynamics to the single-excitation manifold of the addressed transition. Let $x(t)$ be the sender qutrit amplitude in the active state, $u(t)$ the sender transmission-resonator amplitude, $v(t)$ the receiver transmission-resonator amplitude, and $y(t)$ the receiver qutrit amplitude in the corresponding active state.

The amplitude equations follow directly from the cascaded input-output boundary condition. For a transmission resonator $j = A, B$ coupled radiatively to the link, the resonant input-output relation is

$$\hat{b}_{\text{out},j}(t) = \hat{b}_{\text{in},j}(t) + \sqrt{\kappa_j} \hat{a}_j(t), \quad (\text{S38})$$

where \hat{a}_j is the transmission-resonator annihilation operator. The sender input is vacuum, while the receiver input is the attenuated sender output,

$$\hat{b}_{\text{in},B}(t) = \sqrt{\eta_c} \hat{b}_{\text{out},A}(t), \quad (\text{S39})$$

with the propagation phase absorbed into the definition of v and g_B . We use the standard cascaded-systems quantum-trajectory construction [25, 26]. The non-Hermitian Hamiltonian below is the no-jump generator associated with the output and loss channels. In the single-excitation subspace,

$$\hat{H}_{\text{eff}} = \hat{H}_{\text{sys}} + \hat{H}_{\text{casc}} - \frac{i\hbar}{2} \left(\hat{L}_{\text{out}}^\dagger \hat{L}_{\text{out}} + \hat{L}_{\text{loss}}^\dagger \hat{L}_{\text{loss}} \right), \quad (\text{S40})$$

where

$$\begin{aligned} \frac{\hat{H}_{\text{sys}}}{\hbar} &= g_A(t) \left(\hat{a}_A^\dagger \hat{\sigma}_A^- + \hat{a}_A \hat{\sigma}_A^+ \right) + g_B(t) \left(\hat{a}_B^\dagger \hat{\sigma}_B^- + \hat{a}_B \hat{\sigma}_B^+ \right), \\ \frac{\hat{H}_{\text{casc}}}{\hbar} &= \frac{i}{2} \sqrt{\eta_c \kappa_A \kappa_B} \left(\hat{a}_A^\dagger \hat{a}_B - \hat{a}_B^\dagger \hat{a}_A \right), \\ \hat{L}_{\text{out}} &= \sqrt{\eta_c \kappa_A} \hat{a}_A + \sqrt{\kappa_B} \hat{a}_B, \quad \hat{L}_{\text{loss}} = \sqrt{(1 - \eta_c) \kappa_A} \hat{a}_A. \end{aligned} \quad (\text{S41})$$

Here \hat{L}_{out} is the output field after the receiver and \hat{L}_{loss} represents channel loss between the two nodes. The no-jump evolution accounts for the conditional amplitude loss into these channels even before the capture pulse is chosen. Expanding Eq. (S40) cancels the reciprocal $\hat{a}_A^\dagger \hat{a}_B$ term and leaves only the directional drive $\hat{a}_B^\dagger \hat{a}_A$, giving

$$\begin{aligned} \frac{\hat{H}_{\text{eff}}}{\hbar} &= g_A(t) \left(\hat{a}_A^\dagger \hat{\sigma}_A^- + \hat{a}_A \hat{\sigma}_A^+ \right) + g_B(t) \left(\hat{a}_B^\dagger \hat{\sigma}_B^- + \hat{a}_B \hat{\sigma}_B^+ \right) \\ &\quad - \frac{i\kappa_A}{2} \hat{a}_A^\dagger \hat{a}_A - \frac{i\kappa_B}{2} \hat{a}_B^\dagger \hat{a}_B - i\sqrt{\eta_c \kappa_A \kappa_B} \hat{a}_B^\dagger \hat{a}_A. \end{aligned} \quad (\text{S42})$$

The last term is the unidirectional drive of the receiver resonator by the sender output field; it is the term that would be absent in a bidirectional normal-mode Hamiltonian. In these equations $\hat{\sigma}_j^- = |g_j\rangle \langle s_j|$ is the effective lowering operator of the addressed sideband, with $s = e$ for $e0g1$ and $s = f$ for $f0g1$. The four basis states in the single-excitation manifold are

$$\begin{aligned} |x\rangle &= |0_A, s_A; 0_B, g_B\rangle, \quad |u\rangle = |1_A, g_A; 0_B, g_B\rangle, \\ |v\rangle &= |0_A, g_A; 1_B, g_B\rangle, \quad |y\rangle = |0_A, g_A; 0_B, s_B\rangle, \end{aligned} \quad (\text{S43})$$

where the first and third entries are the sender and receiver transmission-resonator photon numbers, and the second and fourth entries are the sender and receiver qutrit states. Thus x is the sender qutrit excitation, u the emitted photon stored in the sender transmission resonator, v the photon stored in the receiver transmission resonator, and y the captured receiver qutrit excitation. Applying $d|\psi\rangle/dt = -i\hat{H}_{\text{eff}}|\psi\rangle/\hbar$ to the no-jump state

$$|\psi(t)\rangle = x(t)|x\rangle + u(t)|u\rangle + v(t)|v\rangle + y(t)|y\rangle \quad (\text{S44})$$

gives, in the resonant rotating frame,

$$\begin{aligned}
\dot{x} &= -ig_A(t)u, \\
\dot{u} &= -\frac{\kappa_A}{2}u - ig_A(t)x, \\
\dot{v} &= -\frac{\kappa_B}{2}v - \sqrt{\eta_c\kappa_A\kappa_B}u - ig_B(t)y, \\
\dot{y} &= -ig_B(t)v,
\end{aligned} \tag{S45}$$

where $g_A(t)$ and $g_B(t)$ are the sender and receiver sideband couplings, κ_A and κ_B are the radiative linewidths of the two transmission resonators, and η_c is the channel efficiency. Perfect absorption imposes the output-field cancellation condition

$$\xi_{\text{out}}(t) = \sqrt{\eta_c\kappa_A}u(t) + \sqrt{\kappa_B}v(t) = 0, \tag{S46}$$

This is the dark-output condition: the receiver resonator field destructively interferes with the attenuated sender field so that no outgoing photon remains after the receiver. It is the input-output version of time-reversed photon capture [21, 22, 25, 26].

We choose the phase convention $u(t) = -iq_A(t)$ and $v(t) = iq_B(t)$, with real mode amplitudes q_A and q_B . Equation (S46) then gives

$$q_B(t) = \sqrt{\frac{\eta_c\kappa_A}{\kappa_B}}q_A(t), \tag{S47}$$

and Eq. (S45) becomes

$$\begin{aligned}
\dot{x} &= -g_Aq_A, \\
\dot{q}_A &= g_Ax - \frac{\kappa_A}{2}q_A, \\
\dot{q}_B &= \sqrt{\eta_c\kappa_A\kappa_B}q_A - \frac{\kappa_B}{2}q_B - g_By, \\
\dot{y} &= g_Bq_B.
\end{aligned} \tag{S48}$$

Therefore, once a smooth sender-resonator mode $q_A(t)$ is chosen, the required sideband controls follow analytically:

$$\begin{aligned}
g_A(t) &= \frac{\dot{q}_A + \kappa_Aq_A/2}{x(t)}, \\
g_B(t) &= \frac{\sqrt{\eta_c\kappa_A\kappa_B}q_A - \kappa_Bq_B/2 - \dot{q}_B}{y(t)}.
\end{aligned} \tag{S49}$$

The remaining amplitudes are fixed by probability conservation in the cascaded no-jump

dynamics,

$$\begin{aligned} x^2(t) &= 1 - q_A^2(t) - \kappa_A \int_{t_i}^t q_A^2(t') dt', \\ y^2(t) &= -q_B^2(t) + \int_{t_i}^t [2\sqrt{\eta_c \kappa_A \kappa_B} q_A(t') q_B(t') - \kappa_B q_B^2(t')] dt'. \end{aligned} \quad (\text{S50})$$

This construction is the finite-resonator analogue of choosing an emitted photon mode and solving for the capture pulse that cancels the outgoing field.

For REG, the two primitives are generated in the physical order $e0g1$ followed by $f0g1$. A strictly zero-start receiver pulse produces a large initial control when $y(t)$ is still very small in Eq. (S49). We therefore use a finite smooth precursor before the main capture window. The sender mode for primitive $j \in \{e, f\}$ is parameterized as

$$q_{A,j}(t) = A_j \sigma_j^{\alpha_j} (1 - \sigma_j)^{\beta_j}, \quad \sigma_j = \left[1 + \exp\left(-\frac{t - t_{c,j}}{\tau_j}\right) \right]^{-1}, \quad (\text{S51})$$

over the finite support $t_{\text{on},j} < t < t_{\text{off},j}$, and is zero outside this support. The time $t_{i,j}$ marks the start of the plotted receiver-capture waveform, not the beginning of the analytic mode: the interval $t_{\text{on},j} < t < t_{i,j}$ is a weak precursor that prepares a finite receiver amplitude, and the interval after the nominal capture waveform is retained only to make the turn-off smooth. With this convention $g_B(t_{i,j})$ can be finite without introducing a sharp initial spike. The normalization is set by the desired partial-transfer probability,

$$\kappa_A \int_{t_{\text{on},j}}^{t_{\text{off},j}} q_{A,j}^2(t) dt = p_j. \quad (\text{S52})$$

For the lossless maximally entangled REG target, $p_e = 1/3$ for the $e0g1$ branch and $p_f = 1/2$ for the subsequent $f0g1$ branch, where p_f is conditional on the population left after the first partial transfer. The shape parameters and support endpoints can then be optimized within this analytic family, while Eqs. (S49)–(S50) provide the corresponding $g_A(t)$ and $g_B(t)$ without replacing the model by an effective decay rate.

For qutrit state transfer, the corresponding optimized-pulse projection is simpler because the target is complete transfer rather than a partial-transfer interference state. We therefore use the unwidowed sech pulse $g(t) = g_0 / \cosh[(t - t_0)/\tau]$ with $g_0/2\pi = 1/(2\pi\tau) = 5$ MHz and the source-notebook timing convention used in Sec. IV B. Inserted into the full cascaded model with $\eta_c = 0.98$, $T_1 = 50 \mu\text{s}$, Markovian $T_\phi = 20 \mu\text{s}$ and no additional internal transmission-resonator loss, this qutrit-transfer sequence gives a mean transferred-state fidelity of 0.968 and a qutrit process fidelity of 0.948.

In the representative REG projection used in the main-text discussion, the waveform start is defined after the weak analytic precursor, so the receiver capture controls begin at finite coupling: $g_{B,\epsilon 0g1}(0)/2\pi = 2.87$ MHz and $g_{B,f0g1}(0)/2\pi = 3.52$ MHz. The full 200 ns waveform satisfies $g_{\max}/2\pi = 3.95$ MHz and ends with receiver couplings below 1 MHz. Inserted into the same pulse-level cascaded model with the same projected device parameters, this inverse-designed REG sequence gives $F = 0.939$, $\mathcal{N} = 0.909$, $C = 2.718$ bits and $I_3 = 2.688$. These numbers are used as a forward-looking device-improvement estimate, not as an additional experimental benchmark.

D. Simulation error budget for qutrit transfer and REG

To identify the dominant limitations in the present pulse-level model, we repeated the Fig. 3 qutrit-transfer and Fig. 4 REG simulations while adding the calibrated error channels one at a time. The first row of Table S6 keeps the experimentally used pulse sequence and pulse amplitudes, but removes photon loss, internal resonator loss, qutrit relaxation and dephasing. This row therefore includes coherent-control imperfections of the calibrated sine-pulse sequence. The following rows add, in order, finite channel efficiency η_c , internal transmission-resonator loss κ_{int} , measured qutrit T_1 , and the quasi-static $1/f$ -like dephasing ensemble. This is a cumulative simulation budget rather than a fit with independent free parameters.

TABLE S6: **Simulation error budget for qutrit transfer and REG.** The first line is the coherent-control result obtained with the calibrated pulse sequence but with $\eta_c = 1$, $\kappa_{\text{int}} = 0$, no qutrit relaxation and no dephasing. Subsequent lines add the physical error channels cumulatively.

Model	QST state F	QST process F	REG F	\mathcal{N}	C (bits)	I_3
Coherent control only	0.969	0.956	0.918	0.879	2.667	2.666
+ channel loss	0.927	0.896	0.870	0.808	2.443	2.531
+ resonator internal loss	0.925	0.893	0.868	0.806	2.434	2.526
+ qutrit T_1	0.905	0.870	0.842	0.768	2.308	2.448
+ quasi-static dephasing	0.895	0.841	0.834	0.756	2.242	2.417

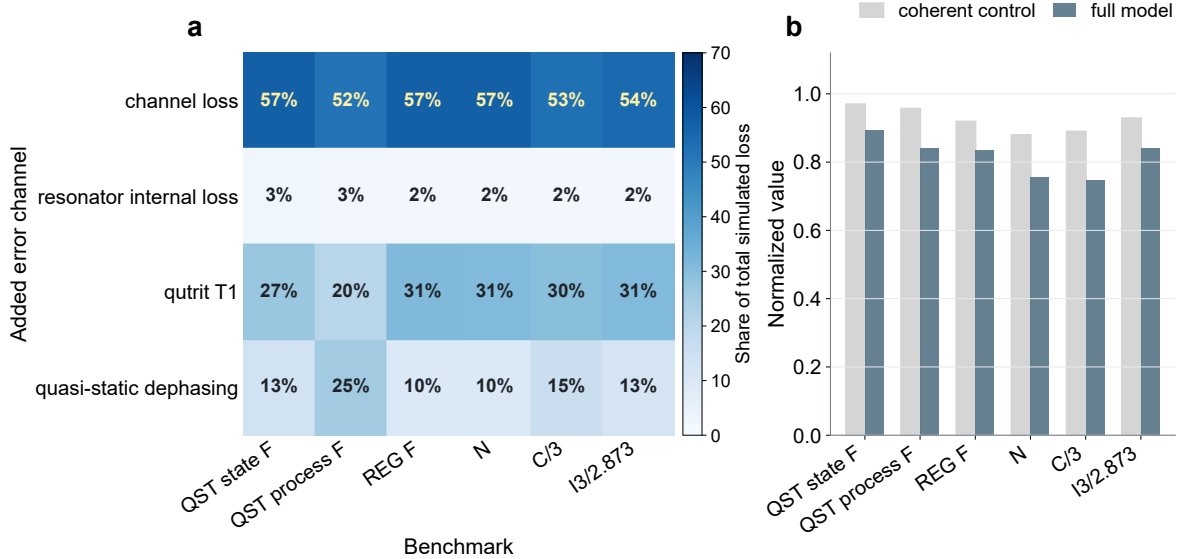


FIG. S14: **Simulation error budget for qutrit transfer and REG.** (a) Incremental contribution of each added error channel to the total simulated loss between the coherent-control row and the full-model row in Table S6. (b) Normalized coherent-control and full-model values for the same benchmarks. Capacity is normalized by 3 bits and I_3 by the ideal qutrit CGLMP value 2.873. For the REG nonlinear metrics, the error budget uses the same averaged-density-matrix convention as the main-text Fig. 4 simulation: the quasi-static density matrices are averaged before evaluating \mathcal{N} , C , and I_3 .

The budget shows two different regimes. For qutrit state transfer, finite channel efficiency gives the largest single drop in both the mean transferred-state fidelity and the process fidelity. The measured qutrit T_1 is the next largest contribution, while internal resonator loss is small at the present $\kappa_{\text{int}}/2\pi$ values. The quasi-static dephasing ensemble has a modest effect on the average state fidelity, but a larger effect on the process fidelity because the process matrix is sensitive to coherent phase errors across the full input-state set.

For REG, the dominant simulated limitations in this convention are finite channel efficiency and qutrit relaxation, while quasi-static dephasing gives a smaller but still phase-sensitive reduction. For the nonlinear entanglement and information metrics in this diagnostic table, we use the same averaged-density-matrix convention as in the main-text Fig. 4 comparison: the density matrices from the quasi-static detuning ensemble are averaged before \mathcal{N} , C , and I_3 are evaluated. This shot-mixed convention gives a stricter estimate of how intra-block phase wandering would reduce the reconstructed two-qutrit resource than

averaging nonlinear metrics over independently phase-stable trajectories. In this limit, quasi-static dephasing reduces the negativity, dense-coding capacity and I_3 , which depend on the phase-sensitive interference terms in the logical qutrit Bell basis. This analysis supports the device-improvement priorities inferred from the data: increasing the channel efficiency, extending qutrit T_1 , reducing low-frequency phase noise, and replacing the experimental sine pulses by REG waveforms designed in the full cascaded model should provide the largest immediate gains, while lower internal transmission-resonator loss gives a smaller but still systematic improvement.

-
- [1] Li, X. *et al.* On-demand shaped-photon emission based on a parametrically modulated qubit. *Physical Review Applied* **23**, 024019 (2025).
- [2] Houck, A. *et al.* Controlling the spontaneous emission of a superconducting transmon qubit. *Physical review letters* **101**, 080502 (2008).
- [3] Reed, M. D. *et al.* Fast reset and suppressing spontaneous emission of a superconducting qubit. *Applied Physics Letters* **96** (2010).
- [4] Bronn, N. T. *et al.* Broadband filters for abatement of spontaneous emission in circuit quantum electrodynamics. *Applied Physics Letters* **107** (2015).
- [5] Yan, H. *et al.* Broadband bandpass purcell filter for circuit quantum electrodynamics. *Applied Physics Letters* **123**, 134001 (2023).
- [6] Magnard, P. *et al.* Fast and unconditional all-microwave reset of a superconducting qubit. *Phys. Rev. Lett.* **121**, 060502 (2018).
- [7] Kurpiers, P. *et al.* Deterministic quantum state transfer and remote entanglement using microwave photons. *Nature* **558**, 264–267 (2018).
- [8] Magnard, P. *et al.* Microwave quantum link between superconducting circuits housed in spatially separated cryogenic systems. *Physical Review Letters* **125**, 260502 (2020).
- [9] da Silva, M. P., Bozyigit, D., Wallraff, A. & Blais, A. Schemes for the observation of photon correlation functions in circuit qed with linear detectors. *Phys. Rev. A* **82**, 043804 (2010).
- [10] Caves, C. M. Quantum limits on noise in linear amplifiers. *Phys. Rev. D* **26**, 1817–1839 (1982).
- [11] Peres, A. Separability criterion for density matrices. *Physical Review Letters* **77**, 1413–1415 (1996).
- [12] Vidal, G. & Werner, R. F. Computable measure of entanglement. *Physical Review A* **65**, 032314 (2002).
- [13] Horodecki, R., Horodecki, P., Horodecki, M. & Horodecki, K. Quantum entanglement. *Reviews of Modern Physics* **81**, 865–942 (2009).
- [14] Bennett, C. H. & Wiesner, S. J. Communication via one- and two-particle operators on Einstein-Podolsky-Rosen states. *Physical Review Letters* **69**, 2881–2884 (1992).
- [15] Horodecki, M., Horodecki, P., Horodecki, R., Leung, D. W. & Terhal, B. M. Classical capacity of a noiseless quantum channel assisted by noisy entanglement. *Quantum Information and*

- Computation* **1**, 70–78 (2001).
- [16] Bowen, G. Classical information capacity of superdense coding. *Physical Review A* **63**, 022302 (2001).
- [17] Collins, D., Gisin, N., Linden, N., Massar, S. & Popescu, S. Bell inequalities for arbitrarily high-dimensional systems. *Physical Review Letters* **88**, 040404 (2002).
- [18] Terhal, B. M. & Horodecki, P. Schmidt number for density matrices. *Physical Review A* **61**, 040301 (2000).
- [19] Johansson, J., Nation, P. & Nori, F. Qutip: An open-source python framework for the dynamics of open quantum systems. *Computer Physics Communications* **183**, 1760–1772 (2012).
- [20] Johansson, J., Nation, P. & Nori, F. Qutip 2: A python framework for the dynamics of open quantum systems. *Computer Physics Communications* **184**, 1234–1240 (2013).
- [21] Korotkov, A. N. Flying microwave qubits with nearly perfect transfer efficiency. *Physical Review B* **84**, 014510 (2011).
- [22] Wenner, J. *et al.* Catching time-reversed microwave coherent state photons with 99.4% absorption efficiency. *Physical Review Letters* **112**, 210501 (2014).
- [23] Pechal, M. *et al.* Microwave-controlled generation of shaped single photons in circuit quantum electrodynamics. *Physical Review X* **4**, 041010 (2014).
- [24] Srinivasan, S. J. *et al.* Time-reversal symmetrization of spontaneous emission for quantum state transfer. *Physical Review A* **89**, 033857 (2014).
- [25] Gardiner, C. W. Driving a quantum system with the output field from another driven quantum system. *Physical Review Letters* **70**, 2269–2272 (1993).
- [26] Carmichael, H. J. Quantum trajectory theory for cascaded open systems. *Physical Review Letters* **70**, 2273–2276 (1993).